Study on Generation Process and Spatial Configuration of RA-I Mechanoreceptor

2018

PHAM QUANG TRUNG

Study on Generation Process and Spatial Configuration of RA-I Mechanoreceptor

by

PHAM QUANG TRUNG

A dissertation submitted to the Department of Engineering Physics, Electronics and
Mechanics, Graduate School of Engineering of Nagoya Institute of Technology
in partial fulfillment of the requirements for the degree of
Doctor of Engineering

Abstract

RA-I receptor plays an important role in human haptic perception, detecting the stimuli that produce minute skin motion (fluttering, slipping, micro-geometric surface, low-frequent vibration). The high-level understanding of human tactile sensing is convinced to provide important hints for tactile sensor design by which raises the level of tactile sensitivity and acuity of robots to human range. This study was motivated by the idea to look for such hints through investigating the poorly known generation process and spatial configuration of RA-I tactile receptors. We expect to find the potential use of this knowledge in producing micro tactile sensors densely and designing high-sensitive sensor cover effectively. However, both topics are not well-investigated at the moment. In this study, we conducted a series of experiments to discover these missing pieces. Our approach includes both anatomical method for investigating the generation process of RA-I receptors and simulation method for investigating the effect of spatial configuration on them.

Firstly, we observed the development of RA-I receptor in-vivo by using conventional fluorescent observation on cross-sectioned samples. We confirmed the development process of RA-I receptor in ICR mouse. Consider the limitations of conventional method, we develop a novel method involved with two-photon microscopy and DiO staining technique. The novel method allows us to repeatedly observe the development of RA-I on the same living mouse, which is not possible in traditional methods. Early result of the two-photon imaging of MC during development period leads us to an idea that the development of MC might be triggered globally by the dermal events (for instance, the growth of phalanx, extension of skin).

Secondly, we develop a finite-element model which mimic the three-dimensional configuration of dermal papillae (the location where the RA-I receptor distributed). The strain energy density tends to concentrate more at RA-I receptor, in comparison with a model with two-dimensional configuration of dermal papillae. In addition, this mechanical response at RA-I receptor also appears to help discerning the spatial configuration of similar indenters. In term of tactile sensor design, this finding could

help improve the elastic cover which usually reduces the spatial resolution of the sensor.

Thirdly, we seek an interpretation of the neurophysiological phenomena where the RA-I afferent (innervated into RA-I receptor) fails to represents the stimulus with the width less than 3 mm. We extended the previously developed model of skin with a transduction layer and synthetic sub-model. The implementation of synthetic sub-model is based on the fact that a single RA-I afferent usually innervates a number of RA-I mechanoreceptors. The output of synthetic sub-model appears to be well-fitted to the neurophysiological data. Therefore, the model can be used for further investigating the mechanism underlying the population response of RA receptor to many types of stimulus such as depressed patterns, gratings, slipping. This finding also suggests the role of branching method in signal pre-processing process at the receptor level.

Acknowledgments

I would like to thank many people for their support and encouragement during my study.

First, I would like to express my gratitude to my advisor Professor Akihito Sano for his guidance and giving me a chance to set my heart on becoming a researcher.

I would like to extend my gratitude to the members of the thesis committee: Prof. Manabu Yamada for his constructive comments and discussions, Associate Professor Masamichi Sakaguchi for his helpful ideas and comment, and Professor Takaki Miyata (Nagoya University) for his guidance, insightful comments, and encouragement, and for giving me the precious opportunity to extend this present study into imaging-neuroscience field.

I would like to thank Associate Professor Yoshihiro Tanaka for the productive research environment and precious comments.

I would like to thank Assistant Professor Takayuki Hoshi for his impassioned discussions, encouragement and guidance.

I would like to thank the members and the staff of the Sano-Tanaka Laboratory: Tomohiro Fukuda, Ly Hoang Hiep,... for exciting work environment and their excellent supports.

My heartfelt thanks to the members and staff of Miyata Laboratory: Assistant Professor Takumi Kawaue, Technical Assistant Makoto Masaoka for their excellent technical assistance, thoughtful discussion, and creating a friendly collaboration.

Finally I would like to thank my family and friends for their understanding, support during the present study.

Contents

4 FE Analysis of the effect of 3D configuration on skin mechanics at RA-I receptor 53

5 Analysis of the transduction layer and synthetic sub-model for investigating the RA-I afferent response 73

List of Figures

List of Tables

Chapter 1

Introduction

1.1 Motivation

Haptic perception is an essential cognitive activity for both human and robots to explore the surrounding environment safely and effectively. The mechanoreceptors are the end organs of the sensory system in human skin, which provide to us the tactile feedback from the surrounding environment. One can consider tactile receptors as haptics sensors that transduce the mechanical stimulus into the neural signals. The high level understanding of human tactile sensing is convinced to provide important hints for tactile sensor design by which raises the level of tactile sensitivity and acuity of robots to human range. This study was motivated by the idea to look for such hints through investigating the poorly known generation process and spatial configuration of tactile receptors.

1.2 Background

The mechanoreceptors are located at different layers of skin (i.e. epidermis, dermis, and subcutaneous tissue). They signalize physical properties, such as shape, size, and texture, of an object that is touched and transmit the signal to the brain (Fig. 1-1a). There are four types of mechanoreceptors, namely Pacinian corpuscles, Ruffini endings, Merkel cells, and Meissner corpuscles. Pacinian corpuscles, Ruffini endings,

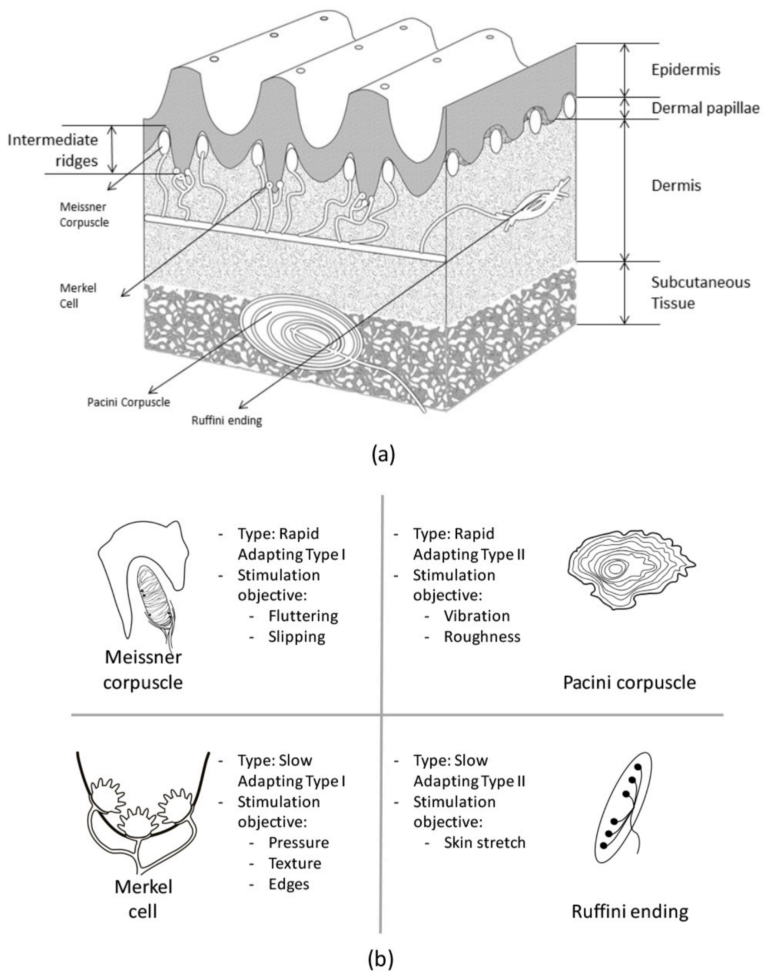

Figure 1-1: (a) Three layers of skin and their related mechanoreceptors. (b) Illustrations and briefs of four types of mechanoreceptors .

Merkel cells, and Meissner corpuscles are the end organs of rapidly adapting type-II mechanoreceptors (RA-II) and slowly adapting type-II mechanoreceptors (SA-II) that correspond to SA-I mechanoreceptors and RA-I mechanoreceptors, respectively. Each type of mechanoreceptors perceives a different kind of sensations (see Fig. 1-1b).

Meissner corpuscles (MC) are located at the dermal papillae, i.e. the middle concave-convex region between epidermis and dermis layers of skin. Meissner corpuscle vigorously responses to low-frequency vibration, and in charge of important sensations such as fluttering and slipping. Among mechanoreceptors, the structure of Meissner corpuscle is the most complex and unique, primarily consisting of spiral axons (spring-like), lamellar cells and outer capsule fibrils (Fig. 1-2). Interestingly,

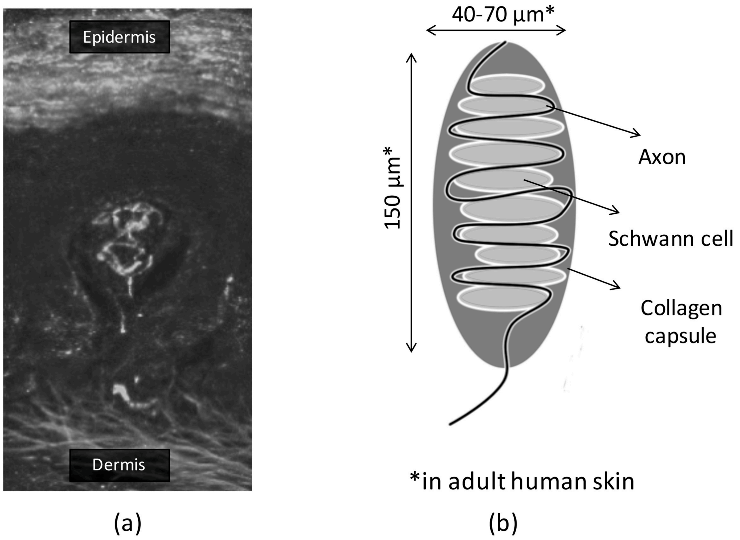

Figure 1-2: (a) Observation of Meissner corpuscle by Confocal Laser Microscopy. (b) Illustration of components of Meissner corpuscle.

despite the complex structure the density of Meissner corpuscle is extremely high in the mammalian fingertip (from 10-24/mm^2).

Various kinds of microscopy can be used for observation of Meissner corpuscle, such as confocal microscopy, transmission electron microscopy (TEM) or scanning electron microscopy (SEM). Although the anatomical shape, distribution, and components of Meissner corpuscle are recognized, they have been mostly determined from observations of fixed tissues. Therefore, knowledge of their development process is limited by the lack of interactive environment and the individual differences among samples.

The theoretical behavior of spring-like axons inside the Meissner corpuscle has drawn interests from a number of authors. For instance, an apex of dermal papillae containing MC can be assumed as a rubber model in which showing MC might be fully stimulated by pressure coinciding with its axis. Meissner corpuscle was also modeled as a spring for investigating the corpuscle characteristic frequency. Despite being mathematically possible, these mechanical behaviors have not been observed yet.

In addition, various simulation studies attempted to investigate the mechanical properties of skin microstructure and their effect on mechanoreceptors (i.e., RA-I, SA-I, RA-II, and SA-II) by using finite element modeling. The models are usually simplified as two-dimensional cross-sections of skin with elastic materials. As the rapid development in computer technology, the number of three-dimensional complex models which include viscoelasticity and hyper-elasticity of skin is growing in recent years. Strangely enough, very few studies have focused on spatial configuration of Meissner corpuscle. Therefore, the role of related surrounding environments (dermal papillae) remains unclear.

1.3 Our objective and approach

Our objective of this study is to provide a deeper insight into the generation process and spatial configuration of Meissner corpuscle, or in other words, RA-I (rapidly adapting type-I) receptor. We expect to find the potential use of this knowledge in producing micro tactile sensors densely and designing high-sensitive sensor cover effectively. Our approach includes both anatomical method and simulation method. Firstly, we use the conventional immunostaining method and confocal laser scanning microscope for observing the in vivo generation process of the RA-I receptor. Considering the limitations of the conventional method, we develop a novel method for observing RA-I receptors in a living mouse repeatedly. Secondly, we simulate the three-dimensional microstructure of skin by finite-element method and estimate the mechanical response at the position of RA-I receptor during indentation. The model is then extended with computational layers to interpreting the neurophysiological phenomena.

1.4 Organization of the Thesis

The thesis is organized as follows.

In Chapter 2, we introduce the related works in RA-I receptor researches. The related works are categorized into three major approaches: anatomical approach, skin mechanics approach, and neurophysiological approach. Our previous work involved with the proposal of tissue-engineering approach is also mentioned.

In Chapter 3, we observe the development of RA-I receptor in-vivo. By using fluorescent observation on cross-sectioned samples, we confirmed the development process of RA-I receptor in ICR mouse. Consider the limitations of conventional method, we develop a novel observation method involved with two-photon microscopy and DiO staining technique. The novel method allows us to repeatedly observe the RA-I receptor on the same living mouse, which is not possible in conventional methods. An early result of the two-photon imaging of MC during development period leads us to an idea that the development of MC might be triggered globally by the dermal events (for instance, the growth of phalanx, the extension of skin). For discussion, we provision the impact of development mechanisms of RA-I receptor in sensor design.

In Chapter 4, we develop a finite-element model which mimic the three-dimensional configuration of dermal papillae (the location where the RA-I receptor distributed). The strain energy density tends to concentrate more at RA-I receptor, in comparison with a model with two-dimensional configuration of dermal papillae. In addition, this mechanical response at RA-I receptor also appears to help discerning the spatial configuration of similar indenters. In term of tactile sensor design, this finding could help improve the elastic cover which usually reduces the spatial resolution of the sensor.

In Chapter 5, we seek an interpretation of the neurophysiological phenomena where the RA-I afferent (innervated into RA-I receptor) fails to represents the stimulus with the width less than 3 mm. We extended the previously developed model of skin with a transduction layer and synthetic sub-model. The implementation of synthetic sub-model is based on the fact that a single RA-I afferent usually innervates a number of RA-I mechanoreceptors. While the mechanical response at RA-I receptor is consistent with previous simulation, the output of synthetic sub-model appears to be fit to the neurophysiological data. Therefore, the model can be used for further investigating the mechanism underlying the population response of RA receptor to many types of stimulus such as depressed patterns, gratings, slipping. This finding also suggests the role of branching method in signal pre-processing process at the receptor level.

Finally, Chapter 6 presents conclusions and directions for future work.

Chapter 2

Related works

We categorize the RA-I receptor related research into three major approaches, i.e. anatomical approach, skin mechanical approach, and neurophysiological approach.

2.1 Anatomical approach

Rapid adapting type I (RA-I) mechanoreceptors, also called Meissner corpuscles (MC), are one kind of fast adapting mechanoreceptor in glabrous skin. They distribute at the dermal papillae, the middle region between epidermis and dermis. The receptors are oval in shape and have the most complex and unique structures among mechanoreceptors, primarily consisting of neural axons, lamellar cells and outer capsule fibrils.

The afferent axonal fibers are derived from dorsal root ganglion and oriented into a spiral shape at the dermal papillae. These fibers are stacked between lamellar cells and both of these structures are covered in a capsule of collagen fibrils [8], [9], [10]. Our understanding of the architecture of the Meissner corpuscle (MC) has followed advancements in microscopy technology. The observation usually involves a combination of silver staining or immunolabelling techniques with microscopy, which include light microscopy (LM) [11, 12, 8, 9, 13, 14] , confocal laser scanning microscopy (CLSM) [10, 15, 16, 17, 18], transmission electron microscopy (TEM) or scanning electron microscopy (SEM) [19, 20, 21, 22] .

Despite knowledge of the physiological and morphological functions of MC (for reviews, see: Munger et al. [23]; Johansson and Vallbo [24]; Esther P. Gardner et al. [25]; Amanda Zimmerman et al. [26]), mechanical transduction is still not understood. Cauna [12] and Takahashi-Iwanaga and Shimoda [22] proposed a mechanism for the response of the axon in MC to mechanical stimuli. Their hypothesis was extended by Kuroki et al. [27] through numerical simulation. However, up to now there have been no practical observations of MC performing work .

2.2 Skin Mechanical approach

Previous studies attempted to investigate the mechanical properties of skin microstructure and their effect on mechanoreceptors by using finite element modeling. Various modeling techniques (from macrostructures to microstructures) were proposed in the biomechanics literature.

In term of macrostructures, a significant model corresponds to the three-dimensional (3D) model of a whole fingertip that was developed based on real human and monkey fingertip geometry by Dandekar et al. [28]. The strain energy density (SED) calculated at the SA-I receptor location of this model was matched with neurophysiological data reported by Phillips and Johnson [29]. A model of the same scale was developed by Gerling et al. [30] with extensive transduction and neural sub-models that convert the SED into neural spikes. The model matched surface deflection in human experiments conducted by Srinivasan [5] and exhibited a good correlation with single afferent responses obtained by Johnson [29] as well as psychophysical results derived by Goodwin [31]. However, fingerprints and other microstructures of skin, such as intermediate ridges, dermal papillae, and fibril structures, were not included in the fore-mentioned macro-structured 3D models.

Results indicate that the microstructures strongly affect the deformation of skin. Hence, an important challenge involves the modeling of skin microstructure to investigate its effect on mechanoreceptors. Maeno et al. [32] developed a two-dimensional (2D) plane strain model based on cross sections of a human fingertip as opposed to using a whole-fingertip model. Their “intermediate ridges” and fingerprints (also called “papillary ridges”) are based on a 2D model developed by Srinivasan [33]. Maeno et al. found that the SED were more concentrated at the apexes and bases of intermediate ridges. Gerling [4] developed a similar model without fingerprints because fingerprints do not appear to affect the distribution of stress and strain at the tips of intermediate ridges (SA-I locations). The model confirmed that the intermediate ridges might focus SED at the location of SA-I receptors but do not affect the SED distribution.

Meanwhile, scarce attention focused on RA-I receptors, which share the intermediate ridge with SA-I receptors. Current models with or without intermediate ridges tend to focus on positions of the SA-I receptors. The 2D model [32] barely exhibited any effect of the intermediate ridge with respect to the stress concentration at the positions of the RA-I receptors.

2.3 Neurophysiological approach

The rapid adapting type-I (RA-I) receptors, type II (RA-II) and slow adapting type-I (SA-I), type-II (SA-II), each respond to different stimulus characteristics (For details, see [34]).

Rapid adapting type-I (RA-I) receptors are believed to be responsible for the detection of stimuli that produce minute skin motion (flutter, slip, microgeometric surface features). The neurophysiological experiments on monkey (for instance, Phillips et al. [35], Blake et al. [7]) showed that the RA-I afferents fail to represent the stimulus with the width less than 3 mm. A recent study from Bensmaia et al.[3] reveals the anisotropy in afferent response to grating orientation. It is unclear whether the skin's mechanics or the specific afferent branching of mechanoreceptors themselves accounted for these phenomena.

2.4 Proposal of tissue engineering approach

A novel approach involves an in vitro systems that approximate the biological activities of the sensory neuron would become the most sustainable method for investigating the mechanical behavior of Meissner corpuscle. Researchers have already examined two other types of mechanoreceptors: Merkel cells, Pacini corpuscles, and their afferent axons in vitro for years (see review in [36]). So far as we know, the in vitro protocol for Meissner corpuscle is not available.

In previous work [37], we proposed the basic concept of tactile sensor based on tissue engineering and some hypotheses of approaching methods. The big idea is to culture the axons which are derived from dorsal root ganglion in-vitro and then make them transformation into Meissner Corpuscle before using them as sensing elements. At present, researchers have found various factors which may change the profile of axon in vitro. The topographical [38], chemical [39], electrical [40], opticals [41, 42, 43, 44] cues and a wide variety of hybrid approaches such as electro-chemical [45], optofluidic flow [46], photo-chemical [47] cues have been employed for the purposes of axonal guidance. Most of these approaches are based on attractive guidance principles. In our concept, the axon is expected to form RA-I receptors through the generation process or the regeneration process. Even though the knowledge about how the generation process occurs in-vivo was lacked, the concept of tactile sensor based on tissue engineering has become the starting point of this presented study.

Chapter 3

Explication of in-vivo development process of RA-I receptor

In the first half of this chapter, we examine the development process of RA-I receptor by using confocal laser scanning microscopy for a small time increment. In the second half, we propose a novel less invasive imaging method that incorporates a staining technique with lipophilic carbocyanine DiOC$_{16}$(3) and two-photon microscopy. This combination allows us to repeatedly observe the Meissner corpuscle in a living mouse which is impossible by the other conventional methods. The results demonstrate the potential of this live-imaging technique as not only an effective alternative observation method but also as a practical interactive approach for examining MC mechanical behavior. The potential uses of our novel imaging method are discussed.

3.1 Introduction

In the conventional approach, sample tissues are sliced into thin serial sections and then fixed before treating with specific antibodies to label individual components. For example, the antibody against neurofilament (NF), protein gene product 9.5 (PGP 9.5), is widely used for immunolabelling axons while protein S-100 and vimentin are reliable markers for lamellar cells, which are derived from Schwann cells [13, 20]. After these operations, the tissue may be deformed or even damaged. Cut sections are usually a few tens of micrometers in thickness and enclosed between a glass plate and an overlaid thin film. Even though cut sections can reach around 70 μm in thickness (thicker than MC dimensions) with a vibratome [18], they tend to contain an entire MC. Furthermore, the inconsistency of samples in time-lapse observation is a limitation of the conventional approach, which makes the analysis problematic. Therefore, an in vivo observation method would be useful for gaining further insight into MC function.

Herrmann [48] proposed noninvasive in vivo reflectance confocal microscopy of MCs without using fluorophores. CLSM can penetrate into tissue to a depth of approximately 50 μm, barely reaching MC locations. This technique shows the density of MCs as discoidal objects inside dermal papillae cavities, which is useful as a neuropathological measurement in, e.g., Charcot-Marie-Tooth disease [49] and HIV [48]. However, the resolution is relatively low and incapable of visualizing the axon morphology inside an MC.

In recent years, two-photon imaging, developed by Denk et al. [50], has all but replaced confocal imaging as the standard method for studying deep tissue. By using near-infrared light, this technique has been shown to penetrate deeper in high scattering tissues such as in vivo skin with high resolution [51], [52]. The samples prepared for two-photon imaging can be both fixed or alive, for imaging of labelled neurons, microglia, astrocytes, blood vessels, dendritic spines and axonal varicosities in living mouse brain [53], [54], [55], [56]. Amit [57] carried out two-photon microscopy of the MC of transgenic mice in a study of diabetic neuropathy.

In the next section, we demonstrate an observation of the development of MC by conventional approach. After that, we propose a in vivo imaging method for MC in the normal living mouse fingertip. This method involves two-photon excitation microscopy and injected DiOC$_{16}$(3) dyes for labelling the neuronal cells. The mice survived after both the injection and observation processes.

3.2 Confocal Laser Scanning Microscopic Observation of MCś development in Mouse

3.2.1 Immunostaining and observation technique

Animal housing and experimental procedures complied with the ethical guideline of the Miyata Laboratory, Department of Anatomy and Cell Biology, Nagoya University Graduate School of Medicine. 8 ICR mice in their post-natal days (from PD4 to PD13) were fixed by perfusion fixation through the heart. The hands were cut off and preserved in 20% Sucrose for 1 day. Then the distal pulp was frozen in Optimal Cutting Temperature (O.C.T) compound (Sakura Finetek USA, Inc.) and cut into 25-μm thick serial sections, parallel to the longitudinal axis of the finger. There were 60 cross-sections in total for each sample.

The primary antibodies PGP 9.5 (UltraClone Ltd., dilution 1:400) was used to staining the MC-related axons. Fluorescence images were captured by a confocal laser scanning microscope (Olympus FV-1000) using 10×, 20×, and 40× objective lens. The laser wavelength was 473 nm. The captured images were post-processed using ImageJ and Microsoft Powerpoint software so that the maximum labeling intensity and contrast were comparable for each sample.

3.2.2 Results

Fig. 3-1 shows the typical development of MC from PD4 to PD13. The dermal papillae were already presented before the development occurred. At PD4, a single axon was found penetrating into an apex of dermal papillae. The tip of innervated axon was already bent at this stage. After a few days (from PD5 to PD7), the number of axons in one apex of dermal papillae increased. It is hard to distinguish which axon was the firstly penetrated one. At PD12, the axons began to gather together, indicating the formation of outer collagen capsule. The egg-like shape of MC was found at PD13 with the width of 15–20 ±1 μm and the length of 20–30 ±1 μm.

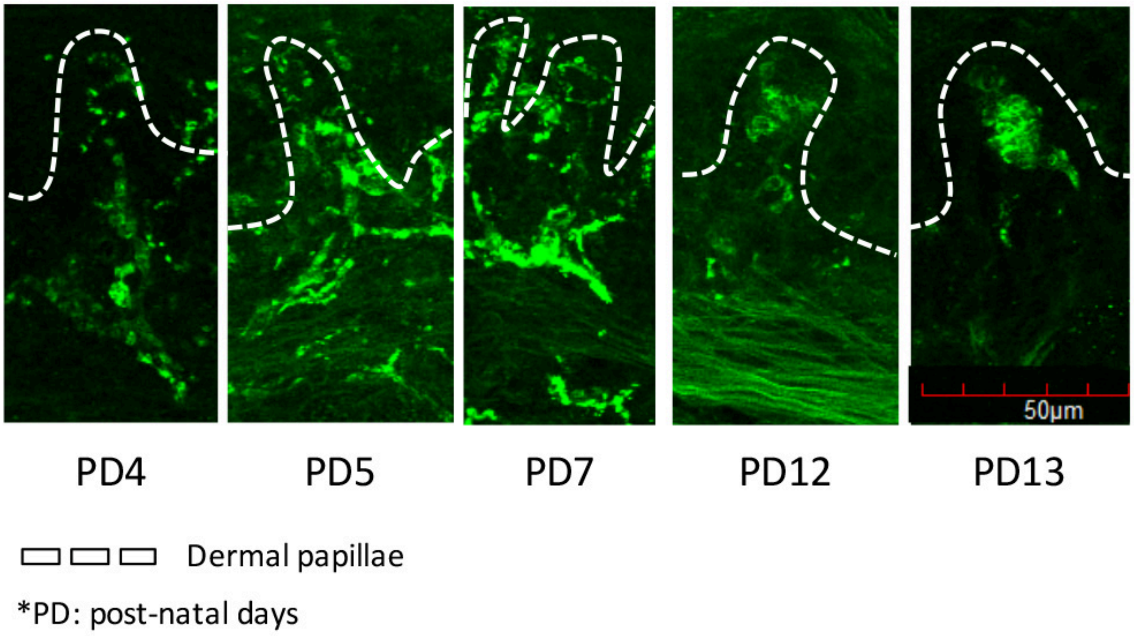

Figure 3-1: Development of Meissner Corpuscle in CLSM observation. The thick green profiles are PGP-9.5 labelled axons. Scale bar = 50 μm.

The development process is consistent with those observed by [13, 19, 58, 11]. The drastically change of MC-like profile is expected because the sample was not the same between stages (one of the limitations of CLSM mentioned in Section 3.1). As the result suggested, the lateral innervated axons appear to rather follow the course of first innervated axon than deform by themselves. Therefore, the deformation of the first innervated axon should be the key point in the whole development of MC.

3.3 The Axonal Origin of Mechanoreceptors and The Concept of Lipophilic Dye Staining

The afferent axons of mechanoreceptors are derived from the sensory neuron body in the dorsal root ganglion (DRG). From the DRG, axons extend down the full length of the arm as a part of the brachial plexus, cross the armpit, elbow and palm, and reach the third phalanx of the finger. The axons continue to branch extensively, and the dividing axons then follow the left and right sides of the phalanges, presenting

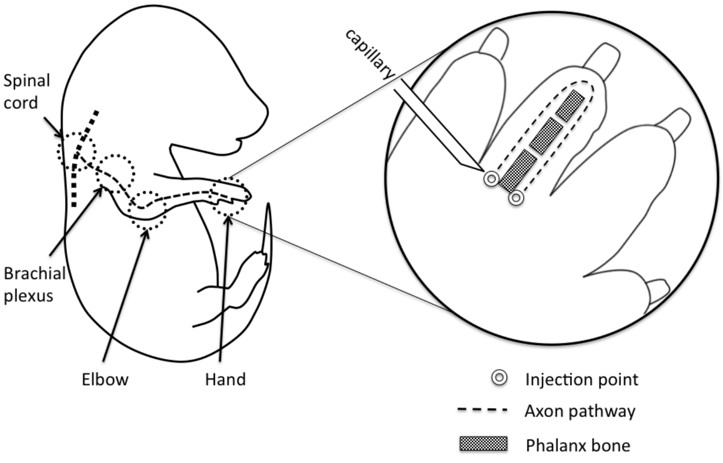

Figure 3-2: Illustration of sensory neural pathway and injection locations.

two parallel lines until the fingertip (for the detailed pathway in the human, see [59]). The axonal pathway of the mouse is illustrated in Fig. 3-2.

A lipophilic dye is injected at one position on the neural pathway and then observed at another distal position (here this is the fingertip where the density of MCs is highest) as the dye diffuses. The lipophilic dyes are the standard neuronal tracers for in vivo tissues and cell research in physicochemistry and biophysics [60], [61], [62], [63]. They are nontoxic and highly fluorescent. After injecting, the lipophilic dye enters the plasma membrane and diffuses laterally, labelling the neuronal projections (axons). They can remain for weeks to allow time-lapse observation [62]. There are many types of lipophilic dyes, e.g., DiI, DiA, DiO, DiD, and DiR. Each has unique fluorescence excitation and emission characteristics. In this study we use $\mathrm{DiOC}_{16}(3)$, 3,3'- Dihexadecyloxacarbocyanine Perchlorate, which is excited by a 484-nm laser with a green emission (501 nm).

The direct injection of lipophilic dye into the DRG was surgically examined by Fischer [64]. However, to be as minimally invasive as possible, all injections in this study were performed without surgery by using anatomical markers. The result of injecting $\mathrm{DiOC}_{16}(3)$ at different locations along the neural pathway is presented in Section 3.4.3. The subjects observed with the two-photon microscope were injected at both sides of the third phalanx using a locating method described below.

3.4 Development of Two-photon Imaging Methods

3.4.1 Staining Technique

$\mathrm{DiOC_{16}(3)}$ crystals (Molecular Probes Inc., USA) were diluted in Ethanol 99.5 (10 mg/mL) solution by an ultrasound vibrator. Next, the container was centrifuged, and then stored in a dark box at normal room temperature (23 °C).

All experiments were conducted with ICR mouse fetuses (from 2 to 33 days postnatal).At 2 postnatal days (PD2), 12 mice were injected simultaneously. The mouse movement during injection was restricted by putting them into an icebox for 3–4 min. The injection device was a Narishige Electric Microinjector IM-31, which consists of three main parts: gas compressor, foot switch and pulled glass capillary injection tip. By adjusting the gas pressure, the device can supply a small amount of dye in each step. In this study, the pressure was set at 40 kPa, equivalent to 2–3 μL/step. The capillary tip was 50–60 μm in diameter and beveled at 65°. Injection was performed manually.

$\mathrm{DiOC_{16}(3)}$ dye was injected directly into both sides of the third phalanx of the point, middle and ring fingers (the thumb and small finger were each only a few millimeters in length and not injected); see Fig. 3-2. Because blood vessels and neural axons track together throughout the body, including in the fingers [59], [65], the closer the injection to the blood vessel, the greater chance that the associated axons will be stained. A halogen backlight was used to expose the position of the blood vessels. The light passed through the almost transparent skin of the mice, displaying parallel red lines on both sides of the phalanx. These lines indicated the position of the blood vessels where the injection should be made.

The mice were then returned to their mothers and monitored until the observation date. The injected mice were left 2 days before pre-checking by a fluorescent stereomicroscope (Leica M165FC). At PD4, they were observed through a 10X ocular lens

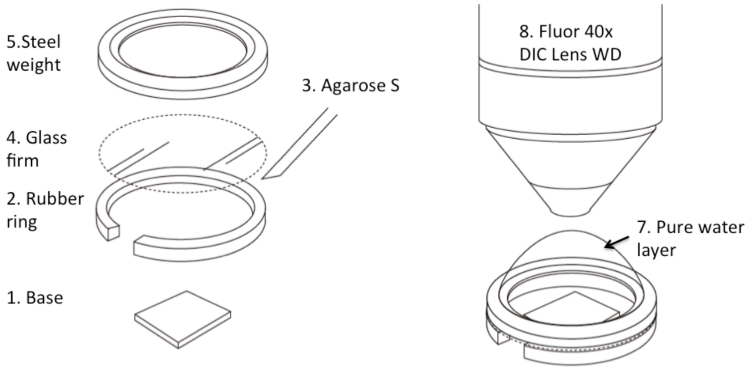

Figure 3-3: Components of the fixation device.

and a 1.6X objective lens to determine whether the DiOC$_{16}$(3) had diffused to the fingertip.

3.4.2 Two-photon Observation Procedure

Mouse anesthesia operation

The mouse was treated with Somnopentyl (diluted in phosphate buffered saline (PBS) solution, 1:10, 510 μL), which caused anesthesia. While anesthetized, the heartbeat still caused micro-vibrations, which were visible under the high-magnification microscope. A fixation device was developed to reduce the influence of these micro-vibrations (Fig. 3-3).

The mouse finger was laid on a thick square base at the center of a dish, surrounded by a rubber ring (22 mm in diameter), and 5 g of Agarose S Gel powder mixed in 100 mL of PBS solution was heated up to 80 °C in a microwave oven. The Agarose S cooled down to around 40–50 °C at room temperature, and was then dropped into the rubber ring. A thin glass film and steel weight (5.25 g) were placed on top, lightly pushing the hand downward. When the Agarose S reached 36 °C, it began solidifying and thus restricted the movement of the finger. Since the objective lens was of water immersion type, a layer of pure water was added on top. The surface tension kept this layer from leaking out during observation.

Microscope Setting Up

In this study, we captured images using a two-photon microscope and lasers of 900 nm wavelength. The laser power was approximately 2.8 mW, controlled to ±10%. The images were collected from the skin surface to a depth of 150 μm. The image resolution was set at 512 × 512 pixels (0.16 μm pixel width). The stacks of two-photon images were produced from 1 μm serial optical sections.

The image sequence was post-processed by ImageJ software (ver. 2.0, FIJI distribution) [66] for stacking and three-dimensional reconstruction. Axonal tracing in three-dimensional space is performed with the Simple Neurite Tracer plug-in [67].

The observation lasted approximately 1 hour, excluding preparation. We visually checked the miceś respiration and body temperature after observation and warmed the mice up, if necessary, before returning them back to the cage. There were neither signs of burns nor apparent behavioral problems; the mice recovered after a few hours without incident.

Identification of Meissner corpuscles

A profile was identified as an MC by the following criteria: a location within the tips of dermal papillae (at a depth of 100–150 μm from the surface); the long axis approximately perpendicular to the dermal–epidermal junction; the presence of an encapsulated spiral structure; and dimensions in the range of those reported for MCs in mouse specimens (10–30 μm in diameter and less than 35 μm in length [13], [14]). These criteria were adapted from [48] with modification of depth and dimensions for a mouse.

For further examining the observed profiles, we fixed the mice by perfusion fixation through the heart. The distal pulp was frozen in Optimal Cutting Temperature (O.C.T) compound (Sakura Finetek USA, Inc.) and immediately cut with a vibratome into 25-μm thick serial sections, parallel to the longitudinal axis of the finger. The sections were treated with the primary antibodies PGP 9.5 (UltraClone Ltd., dilution 1:400) and S-100B (ProteinTech Ltd., dilution 1:700), separately. Flu-

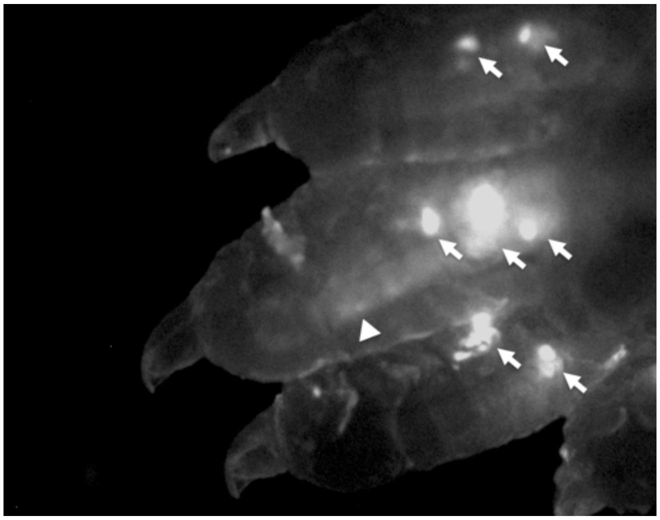

Figure 3-4: DiOC$_{16}$(3) injected mouse fingertip at PD4. Light fluorescent microscopy (488-nm filter). The stained afferent axon of the middle finger shows a white fluorescent line, extending from the base of the finger to the fingertip (arrowhead). The white dots at the base of the fingers (arrows) are the injection locations. The distal pulp of the middle finger is glowing, in contrast to the other fingers.

orescence images were captured by a confocal laser scanning microscope (Olympus FV-1000) using a 40× objective lens with 4× digital zoom). Because the label intensities often differed between the antibodies, the images compiled for illustrative purposes in Fig. 3-9, Fig. 3-10, Fig. 3-13, and Fig. 3-14 were adjusted using ImageJ and Microsoft Powerpoint software so that the maximum labelling intensity and contrast were comparable for each antibody.

3.4.3 Results

Success rate of DiOC$_{16}$(3) staining technique at different positions of sensory neural pathway

This experiment involved 87 PD2 mice. The DiOC$_{16}$(3) dye was injected into the DRG, armpit, elbow, middle palm, and the third phalanx separately.

Fig. 3-4 demonstrates a successful injection, observed at the middle finger of PD4. As the stained axons run in parallel on both sides of the phalanxes, the diffusion of DiOC$_{16}$(3) resulted in two white fluorescent lines, extending from the base to the fingertip of the middle finger (Fig. 3-4). The concentrated dot at the base of the

Table 3.1: Success rate at different injection locations

Position	Number of individuals	Success Rate (%)
DRG	31	0
Armpit	5	0
Middle palm	31	22
The third phalanx (with lamp support)	20	80

finger is where DiOC$_{16}$(3) was injected. The fluorescent intensity is graduated from the base to the fingertip. Unsuccessful injections produced a fluorescent concentration at the base of the fingers only (the other fingers in Fig. 3-4).

Table. 3.1 presents the success rate at each position of the neural pathway, defined as the percentage of fluorescent individuals in one attempt, regardless of the number of fluorescent fingertips per mouse. The only acceptable success rate (80%) was found in the case of injection in the third phalanx.

Two-photon imaging of Meissner corpuscle in living mouse

In mice, the MC attains its mature form at PD22 [19], [13], thus the two-photon imaging was performed at PD33 (the 31st day after injection). This experiment was performed with a Nikon A1RMP microscope and a high magnification lens, Nikon Fluor 40× DIC 0.8W (Nikon Corporation, Tokyo, Japan).

The MC-like profiles were found arranged in a row in dermal papillae (Fig. 3-5) at a depth of 150 μm from the surface, with their long axis oriented vertically. In a dermal papilla, the corpuscle presented alone (Fig. 3-6) or grouped (Fig. 3-7) with a complex spiral shape. Fig. 3-7 demonstrates a single afferent axon branching into several corpuscles. The dividing axon penetrated through the base of the corpuscle and presented discoidal fringed regions along the trajectory (Fig. 3-8a). A corpuscle was selected for further examination by neural tracing image analysis and a three-dimensional reconstruction of 30 serial optical sections (z step of 1 μm; Fig. 3-

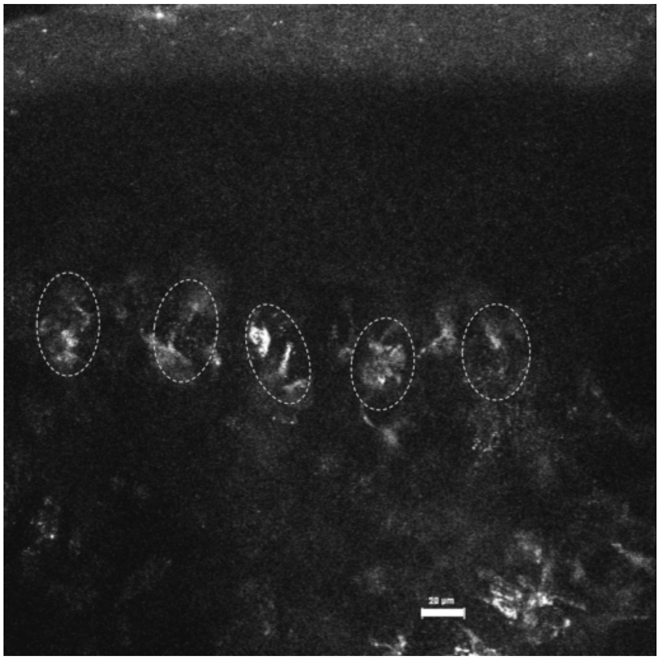

Figure 3-5: A row of Meissner corpuscles (dotted line) in a living PD33 mouse fingertip at a depth of 100 μm from the surface, acquired by a two-photon microscope and 40× water-immersed lens. Scale bar = 20 μm.

8b, 3-8c). Two axons, with diameter varying from 2–4 μm, penetrated into the corpuscle. The corpuscles varied from 20–30 ±1 μm in length and from 10–16 ±1 μm in diameter. These measurements satisfied the criteria described in Section 3.4.2. Fig. 3-8d demonstrates a 60 degrees rotation to the right of the reconstructed MC.

Fig. 3-9a–c show a stack of 46 confocal optical sections (z step of 1 μm) of an MC, post-stained by antibody PGP9.5. The cross section was derived from a DiOC_{16}(3) injected mouse at PD19. The DiOC_{16}(3) dyes remained after fixation but much less intense as in live observation (Fig. 3-9a). The overlaid image revealed the co-expression of the remained DiOC_{16}(3) and post-stained PGP9.5 at the observed MC (Fig. 3-9c).

The other post-stains at PD24 (with S100B) showed that S100B stained profiles also co-existed at the position of DiOC_{16}(3) labelled profiles under low magnification (Fig. 3-10a–c). However, the higher magnification (2× digital zoom) revealed that the S100B profiles associated but not overlapped the DiOC_{16}(3) labelled profiles (Fig. 3-10d–f).

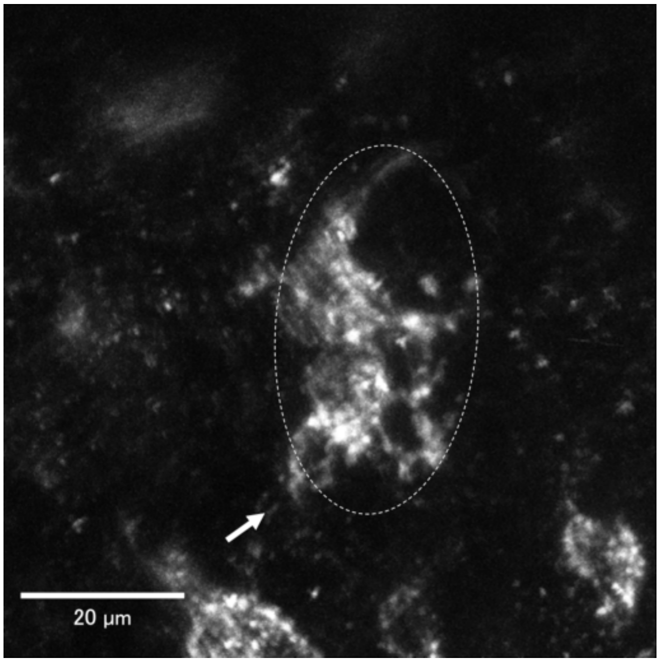

Figure 3-6: Detailed profile of a single Meissner corpuscle (dotted line) labelled with $\mathrm{DiOC}_{16}(3)$, acquired by 40× water-immersed lens and 4× digital zoom. PD33. Z-stack of 20 serial optical sections (z step of 1 μm), two-photon microscopy. The afferent axon penetrates through the base and tortuous course toward the apex (arrow). Scale bar = 20 μm.

Repeated observation of a Meissner corpuscle in a short period

Two mice were repeatedly observed over a short period using an Olympus FV-1200MPE microscope and an Olympus XLPNL25XWMP2 lens (Olympus Corporation, Tokyo, Japan). A type FV10-MRV/G (Olympus) filter was used for capturing the fluorescence of both the collagen (autofluorescence at 440 nm) and the injected $\mathrm{DiOC}_{16}(3)$ (emission at 501 nm). In Fig. 3-11, the autofluorescence of collagen was rendered as red for better contrasting with $\mathrm{DiOC}_{16}(3)$ (green). As a result, the dermal papillae and the other landmarks became recognizable.

Fig. 3-11a–c represents the same fingertip of the same mouse at PD19, PD20 and PD24, respectively. During this period, the size of the fingertip gradually increased while the fluorescent intensity slowly decreased. The location of targeting MC also shifted distally from the position in the first observation (PD19); however, the pattern of $\mathrm{DiOC}_{16}(3)$ and the surrounding landmarks remained. This pattern and the

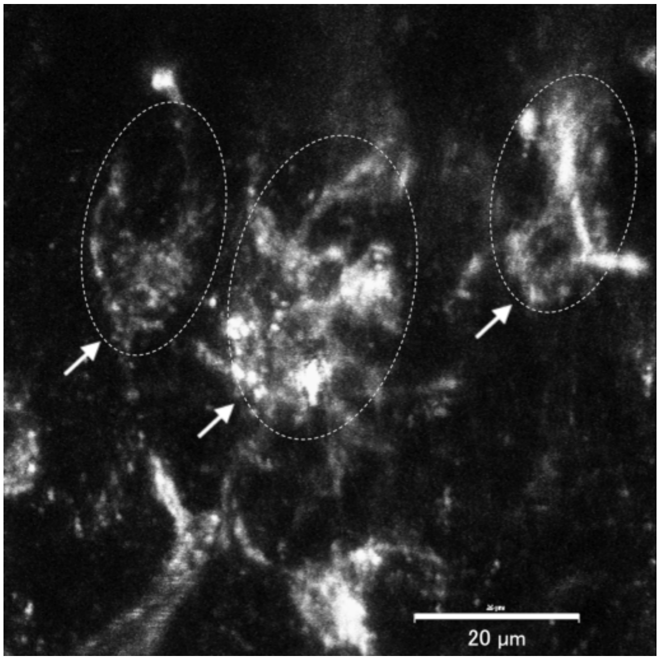

Figure 3-7: Detail profile of grouped Meissner corpuscles (dotted lines) labelled with $\mathrm{DiOC}_{16}(3)$, acquired by 40× water-immersed lens and 4× digital zoom. PD33. Z-stack of 20 serial optical sections (z step of 1 μm), two-photon microscopy. One afferent axon branches into several corpuscles (arrow). The morphology of the neighboring corpuscle is varied. Scale bar = 20 μm.

landmarks helped to track the single MC-like profile (Fig. 3-11d), which appeared to satisfy all the criteria described in Section 3.4.2. The three black circles, which acted as the landmarks, are the cross sections of the tips of dermal papillae.

3.5 Early results of Two-Photon Imaging of MC in development period

In this section, we attempt to use the two-photon imaging methods in observing the development of MC in-vivo. One mouse was observed repeatedly at PD9 and PD16. The procedure is the same as described in Section 3.4. The images were captured by using the Nikon-A1RMP microscope with Nikon Fluor 40× DIC 0.8W lens. The default settings of microscope render the autofluorescence of collagen fiber as blue.

Fig. 3-12a–b represent the axonal profiles at PD9 and PD16, respectively. In-

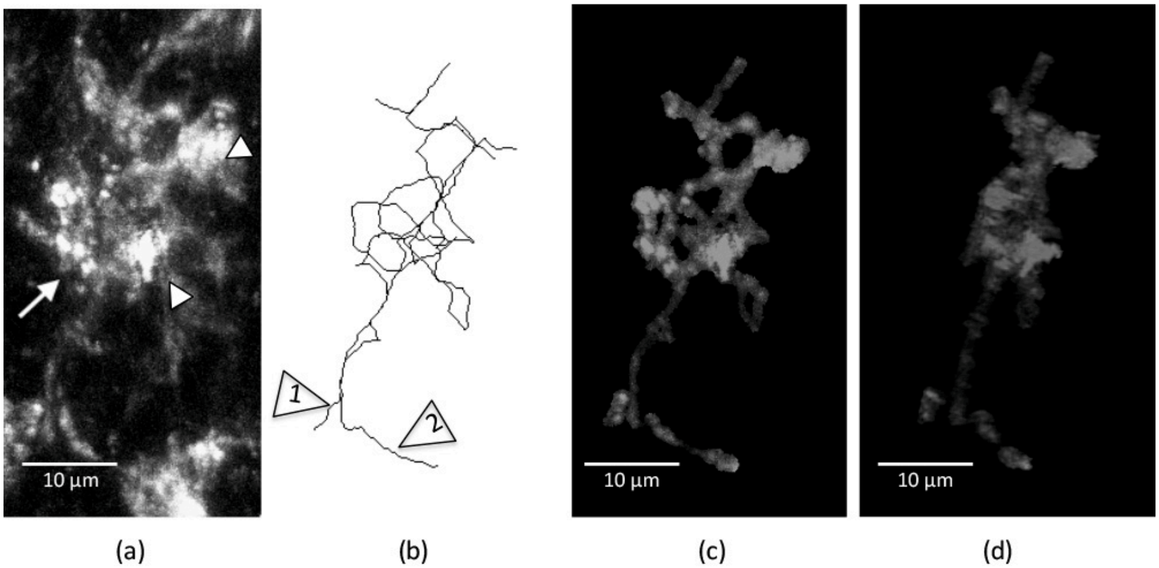

Figure 3-8: Analysis of a single Meissner corpuscle labelled with DiOC$_{16}$(3). (a) An axonal profile of MC. There are two discoids along the course (arrowhead). (b) Axonal course of (a) in three dimensions by ImageJ demonstrates two separate axons penetrating into MC. (c,d) Three-dimensional reconstruction from traced axons confirms the spiral shape of MC. (d) is rotated 60 degrees to the right with respect to (c). Scale bar = 10 μm.

evitably, the two-photon axonal profile highly resembles those observed at the same period in CLSM (from PD7 to PD13 in Section 3.2). The similar profiles at PD16 suggested that the neighbor MCs may mature simultaneously. Even though the development of MC required a more detailed two-photon imaging in small time increments, this result leads us to an idea where dermal events (for instance, the growth of phalanx, the extension of skin) trigger the development of MC globally.

3.6 Discussion

3.6.1 The multiple mechanisms theory of the development of MC

The development of the MC has been extensively investigated in primates and mice [13, 19, 20, 58, 11]. The development period for these two species is different: from 17–24 weeks estimated gestational age to newborn in primates [58], and from newborn to

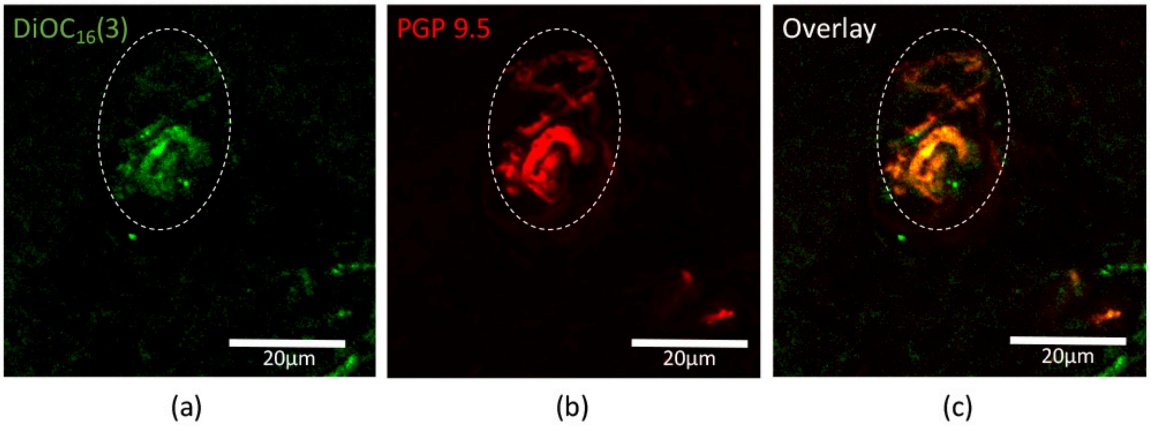

Figure 3-9: Immunofluorescence labelling of MCs in 25 μm thick sections. (a) A remained $DiOC_{16}(3)$ profile (dotted line) after fixation was revealed by green filter. In cut-section, the intensity of background of $DiOC_{16}(3)$ labelling was higher than PGP9.5 labelling. For illustration purpose, the background was suppressed by increasing the contrast and digitally remove lower signals by using Despeckle filter of ImageJ. (b)The PGP9.5 labelled profile was revealed by red filter. (c) Overlaid image, yellow indicate the observed profile was definitively labelled with both $DiOC_{16}(3)$ and primary antibody PGP9.5. Scale bar = 20 μm.

approximately 25 days after birth in mice [19]. The first axon is believed to penetrate into the tip of the dermal papilla, perpendicular to the skin surface. After a period of time, the axon at the tip of the dermal papilla orients parallel to the skin surface, and then becomes spiral. Our observation by both confocal laser scanning method (Fig. 3-1) and two-photon imaging method (Fig. 3-12) confirms this process.

Our observations lead to the thought that the development of MC involves three sequent mechanisms. The first mechanism is for transforming the firstly penetrated straight axon into spiral-like shape (from PD1 to PD4). The second mechanism is for penetration of lateral axons (from PD5 to PD9). The third mechanism is for encapsulating the MC (from PD12 until maturation). Although the details of these three mechanisms are not understood, we would like to discuss their potentials in both technological aspect and scientific aspect as follows.

The first and second mechanisms suggest that the axonal connection (wires) has been established before the formation of tactile receptors (sensing elements). And the formation of tactile receptors should be derived from global dermal events. Ap-

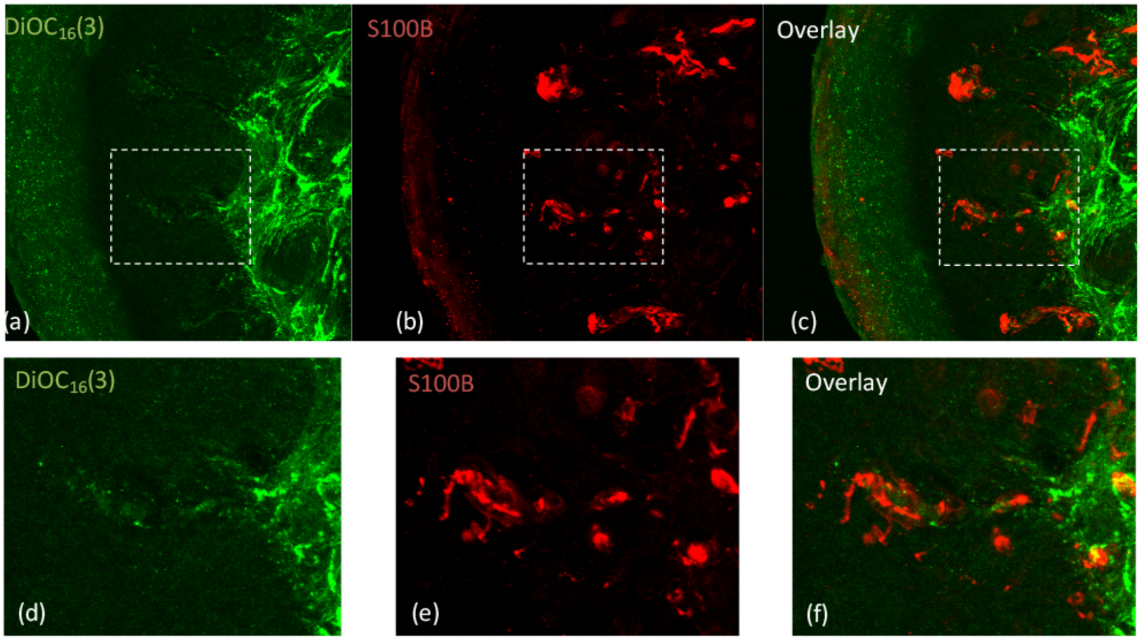

Figure 3-10: A fingertip of PD19 mouse expressed double fluorescence of (a) DiOC16(3) and (b) antibody S100B. (c) is the overlaid image of (a) and (b). The images were acquired with a 40x lens. (d-f) are the 2x digital zoom of the dashed square region in (a-c) respectively. The S100B profile closely associates with the DiO profile.

parently, the first and second mechanism could be the key point to achieve high-density of receptors, reminding that the density of MCs in fingertip is from 12 to 38 receptors/mm^2 [24, 17]. On the other hand, the available tactile sensors usually achieve high-density by producing and implementing every single sensing element before wiring (for instance, [68]), which in contrast to our observations. Therefore, the understanding of the first and second mechanisms of MC development would lead to an efficient way to producing tactile sensor densely.

The third mechanism governs the encapsulation of MC. No one knows precisely why the MC is encapsulated at the first place. While in the case of Pacini corpuscle, it is known that the encapsulation helps improve the receptor sensitivity to dynamic stimulation. Here, we suggest that the encapsulation may tighten the inner of MC, brings the spiral axons closer to each other. Since the computational neuroscience considers the axons (in particular, their neuronal membrane) as equivalent RC circuits, the higher influence between axons is expected. Thus, the axonal response of

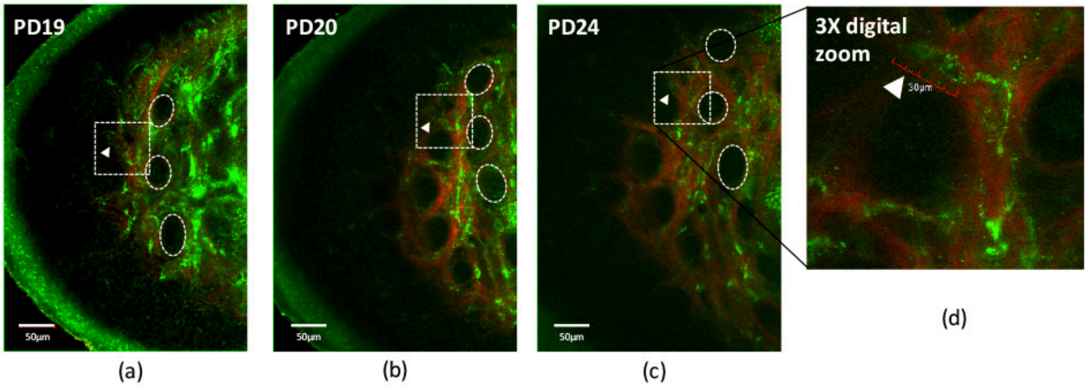

(a) (b) (c) (d)

Figure 3-11: Repeated observations of the same mouse fingertip, stained with $\text{DiOC}_{16}(3)$. The images were obtained with a 25× lens. The white dashed square indicates the tracking range, the white triangle indicates the targeted MC and the white dashed circle indicates the landmarks, which are the cross sections of dermal papillae. (a) presents the fingertip at PD19 with strong fluorescence of $\text{DiOC}_{16}(3)$ as green, and autofluorescence of collagen as red. (b) presents the same fingertip at PD20. (c) presents the same fingertip at PD24. (d) presents the 3× digital magnification of the dashed square in (c) shows an MC, satisfying the criteria described in Section 3.4.2. Scale bar = 50 μm.

MC would be more vigorous.

3.6.2 The use of novel two-photon imaging method

We have developed a novel less-invasive imaging method with lipophilic dye ($\text{DiOC}_{16}(3)$) and two-photon microscopy for capturing the MCs in living mice. The advantage of this method is that the subjects were survived during the operation while displaying the MC profiles. These MCs are more detailed than those acquired by the CLSM method [48]. The 3D reconstruction was additionally demonstrated in Fig. 3-8c, 3-8d. The mice showed no abnormal behavior after injection or observation processes.

The MC-like profiles were consistent with those in previous reports [9], [10]. The axons were innervated from the lower base and branched repeatedly inside the corpuscle without interconnections. The nerve course was tortuous toward the apex with some discoidal portions as reported by Castano et al. [10] and Guinard et al. [18]. Pare et al.[17] described the spatial population of MCs in humans as rows along the

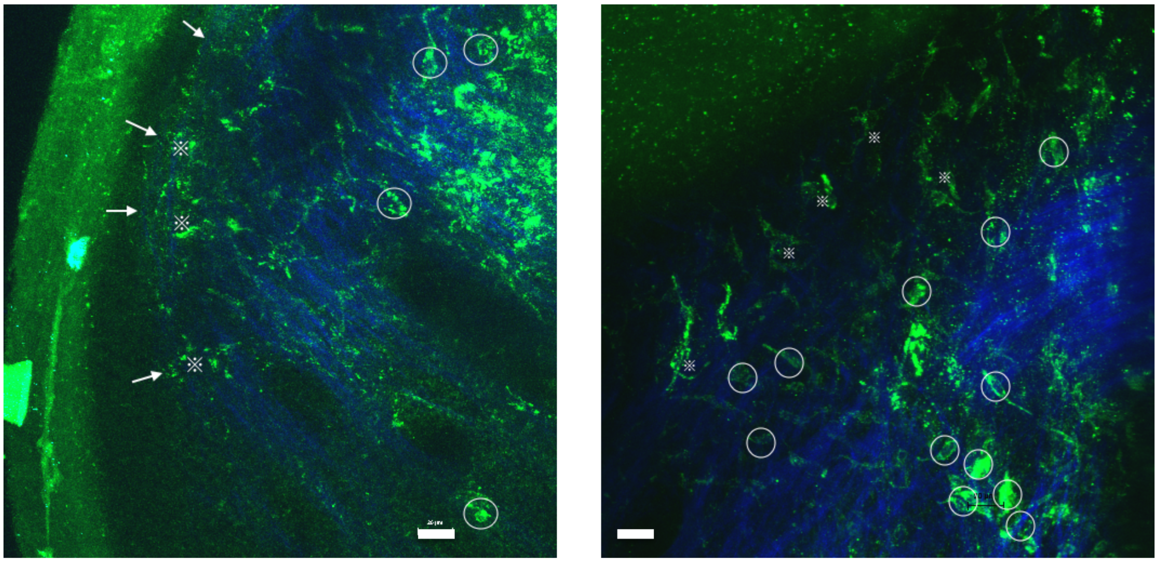

(a) PD9

(b) PD16

Figure 3-12: Two-photon Imaging of MC at (a) PD9 and (b) PD16. The thin green profiles with asterisks are DiOC$_{16}$(3) labelled axons. The blue profiles are auto-fluorescent collagen. The white arrows denote the tips of axon. The white rounds are unknown objects. Scale bar = 20 μm.

fingerprints (epidermal ridges). Surprisingly, the MCs in mice were arranged in a similar manner, although the mouse toe pad is smooth (Fig. 3-5).

The DiOC$_{16}$(3) labelled profiles were shown positive to antibodies PGP 9.5 (Fig. 3-9), which is standard for labelling axons. The DiOC$_{16}$(3) dye consistently remained after fixation though the maximum intensity is lower than in live observation. We suggest the alcoholic component of O.C.T compound used in the post-stain process might have diluted the DiOC$_{16}$(3) dyes. The existence of S100B profiles near the DiOC$_{16}$(3) labelled profiles also strengthens the evidence that they are afferent axons of MC. The S100B profiles did not overlap the DiOC$_{16}$(3) profiles because S100B is mainly found in Schwann cells [69] which usually associated with axons.

To determine whether the neural axon is the only contributor to the observed profiles, we additionally treated the cut sections with primary antibodies for other components, such as the blood vessels (Fig. 3-13). The blood vessels could be accidentally labelled because they were sometimes grazed or possibly impaled during the injection process. Li et al. [70] have demonstrated a method where the direct

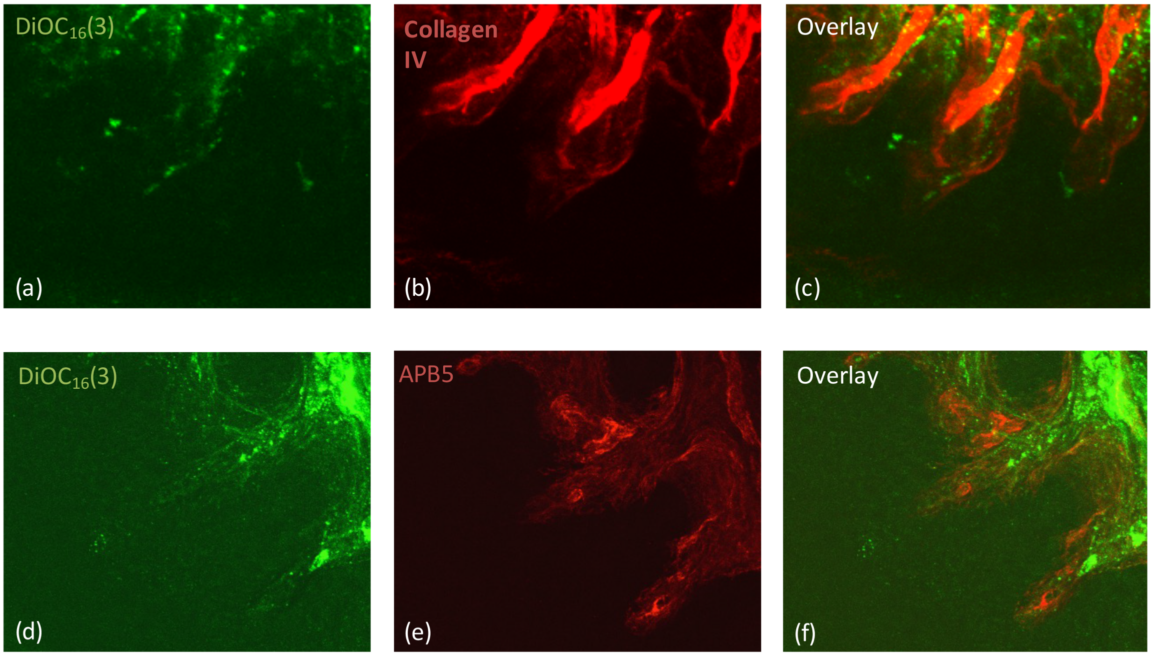

Figure 3-13: Fluorescence of DiOC16(3) and Collagen IV (a-c), and DiOC16(3) and APB5 (d-f) at MC positions, acquired by 40x lens and 4x digital zoom. The DiO profiles are not overlapped both Collagen IV and APB5 profiles.

injection of lipophilic carbocyanine dye labelled the blood vessels. We used two primary antibodies, a rabbit polyclonal antibody collagen IV (Abcam plc., Japan) and a rat monoclonal antibody APB5. The antibody collagen IV labelled the basement membrane of blood vessels while the APB5 labelled the inner smooth muscle of the blood vessels [71]. However, the $\mathrm{DiOC}_{16}(3)$ stained profiles were negative to both antibodies (Fig. 3-13), indicating that the blood vessels did not contribute to the observed profiles in this study.

From our findings we submit that lipophilic dye is useful for labelling the afferent axons in mechanoreceptor research. The injection procedure is simple because the transparent skin of mice reveals the blood vessels with the aid of a halogen lamp backlight. The blood vessels work as indicators for locating the relative position of the associated axon. An injection position closer to the fingertip provides a higher chance of success (Table. 3.1). Injection at a remote position would require more effort (e.g., training with surgery beforehand [64]) and a greater quantity of dye. The dye would also need a longer time to reach the fingertip, because the lateral diffusion rate of dyes was shown as about 6 mm per day in living tissue [62], [72].

We also found that an injected mouse can be repeatedly observed over a period of time. Fig. 3-11 demonstrates 3 observations in 5 days. The development of dimensional and structural aspects of the fingertip can be observed, and a high magnification lens (such as 60× or 100×) can enhance the image details. The capture time should be monitored at regular intervals because the mouse may wake up (anesthesia effect weakened) or die during the observation.

The present study has some limitations. First, the lipophilic dye was shown to only label the neural profiles of MC in living tissue. The other components (lamellar cells and collagen capsule) require different markers or labelling methods, which remain unknown. Second, the injection procedure depends on the skill level of the operator. The glass capillary is fragile and easily clogged as $\mathrm{DiOC_{16}(3)}$ crystals are not completely soluble.

In addition to ethical and cost benefits, our less invasive imaging method also has the following features, which cannot be realized by the cut-section approach.

Observing the development of Meissner corpuscle on the same living mouse

The cut-section approach implies that each observation involves with one different individual. This interchange raises the issue of the consistency of information attributed to individual differences, which can be overcome with our method. The MC can be re-observed in its entirety in small time increments, providing the sequence images at each development state. Neural profiles stained by $\mathrm{DiOC_{16}(3)}$could preserve the fluorescent state for 5 weeks (as injected in PD2 and observable until PD33) in this study (Fig. 3-5-3-7).

There are also a few other issues worth considering. As a mouse grows, the finger becomes larger and the dermis also extends broadly, which is observable even in a single day (Fig. 3-11a, b). Given that the newborn mouse develops rapidly, it is difficult to locate the same MC over time, as both the MCs and their surrounding basement pattern are continuously changing. A different strategy, perhaps involving a new marker, would be required to locate the same MC in each observation.

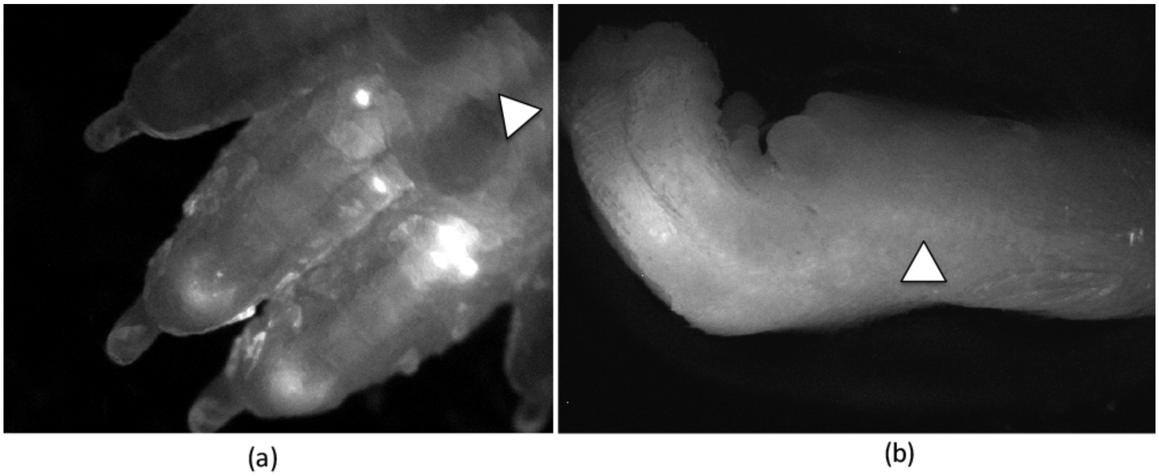

Figure 3-14: Reserve labelling (arrowhead) at (a) the palm and (b) the arm of a PD14 mouse.

Nonetheless, we succeeded in locating the same MC from PD19 to PD24 (Fig. 3-11) because the mouse had almost reached maturity during that period. The surrounding pattern was similar in PD20 and PD24.

Providing mechanical interactive environment during observation

The samples of cut-section approach are usually a few tens of micrometer in thickness and enclosed between a glass plate and an overlaid thin film. The samples are fragile and incapable of mechanical interaction. In our less-invasive imaging method, all the components and the overall form of the finger were preserved (Fig. 3-4, Fig. 3-14). This characteristic allows the subject to receive stimuli for live-observing the transformation of the dermal components. For example, the weight of the metal ring (here 5.25 g) that pushes the fingertip to the base, could be varied, resulting different skin deformations. As MCs mainly respond to dynamic stimuli, stimulation with ramp-and-hold or vibration is challenging. The stimulation might shift the MC targeting position out of the focal plane. In summary, we expect to observe in vivo the three phases of the MC mechanical response, namely the basal, dynamic phase and static phases [22].

Extendable for other subjects and applications

The Aβ nerve fibers from the DRG penetrate not only the MC, but all types of mechanoreceptors, including the Pacini corpuscle, Ruffini corpuscle and Merkel cell. These mechanoreceptors are theoretically observable with our labeling method. This paper focused on the MC because they lie at the shallowest skin position (about 50–150 μm from the surface). Their spiral structure (approximately 10 μm diameter in mice) is also recognizable. The other mechanoreceptors are either located deeper (Pacini corpuscle) or have a nonspecific neural structure (Merkel cell). Criteria based on their own histologic and immunohistochemical characteristics need to be established.

Furthermore, our method can be used on the living monkey and possibly on humans, as the lipophilic dye is nontoxic. This is an advantage over ex vivo methods and transgenic subject methods [57], which cannot be performed on humans for ethical reasons. Previous studies demonstrated changes in shape, size and density of MCs consistent with nervous system diseases, such as HIV neuropathy [48], Charcot-Marie-Tooth disease [49], diabetic neuropathy [57] and Parkinson's disease [73]. Therefore, the present in vivo imaging method could be useful for assisting diagnosis in from laboratory assays.

Another application of in vivo imaging is in microneurography experiments [74]. Microneurography has largely been used in the haptic field for obtaining the neural response of mechanoreceptors. The distinguishing of nerves from other tissues (such as blood vessels) is needed for safer procedures [75]. Our light microscopy observations of mice injected with lipophilic dye revealed that the axons in palmar barely fluoresced (Fig. 3-4, Fig. 3-14), indicating a reserve labeling. The $DiOC_{16}(3)$ could trace back to the neutral body in the DRG. Although the mechanisms underlying the reserve and forward labelling are unknown, the reserve labeling is expected to benefit microneurography experiments as a fiber marking technique.

Chapter 4

FE Analysis of the effect of 3D configuration on skin mechanics at RA-I receptor

Previous studies attempted to investigate the mechanical properties of skin microstructure and their effect on mechanoreceptors by using finite element modeling. However, very few studies have focused on the three-dimensional microstructure of dermal papillae, and this is related to that of RA-I receptors. A gap exists between conventional 2D models of dermal papillae and the natural configuration, which corresponds to a complex and uneven structure with depth. In this chapter, we model the three-dimensional microstructure of dermal papillae, and examine the differences between two-dimensional and three-dimensional aspects of dermal papillae on the strain energy density at receptor positions. The three-dimensional microstructure has a focalizing effect and a localizing effect. Results also reveal the potential usefulness of these effects for tactile sensor design, and this may improve edge discrimination.

4.1 Introduction

Pacinian corpuscles, Ruffini endings, Merkel cells, and Meissner corpuscles are the end organs of rapidly adapting type-II mechanoreceptors (RA-II) and slowly adapting type-II mechanoreceptors (SA-II) that correspond to SA-I mechanoreceptors and RA-I mechanoreceptors, respectively. They are positioned at different depths of the skin (Fig 4-1a). Specifically, SA-I and RA-I receptors share the intermediate region between the epidermis and dermis. As shown in Fig 4-1, the microstructure of the intermediate region between the epidermis and dermis is separated into the following two terms: intermediate ridges that correspond to a typical aspect perpendicular to fingerprints, and dermal papillae that correspond to an aspect parallel to fingerprints. The anatomical components of skin and geometry of ridges are described in [76] and [12].

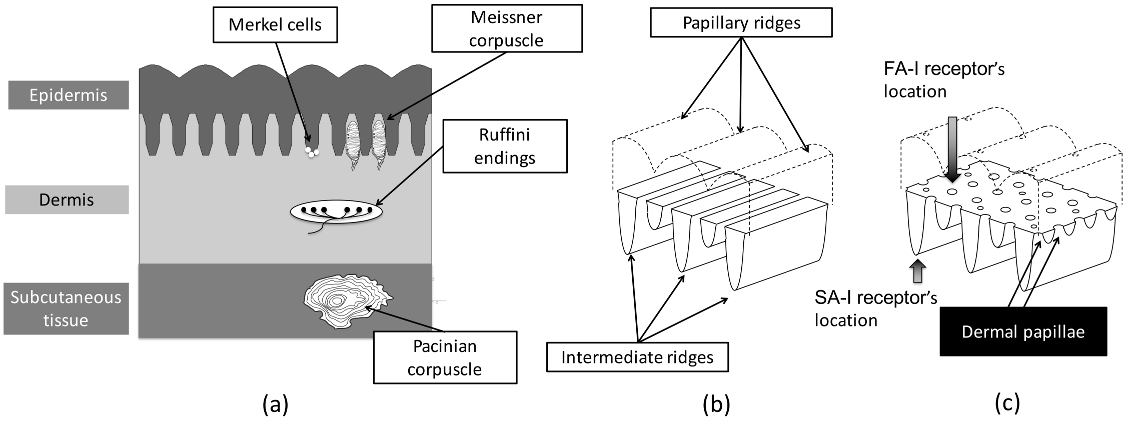

Figure 4-1: (a) Illustration of the skin cross-section and its mechanoreceptors. (b) Depth assumption of a 2D microstructure and (c) Natural configuration of a 3D microstructure according to [1].

There is a paucity of research on the mechanotransduction mechanism by which a tactile stimulus is transformed into a neural signal. Finite-element modeling (FEM) is a reliable method for investigating the mechanical properties of skin components and the manner in which they affect mechanoreceptors.

A potential explanation corresponds to the lack of anatomically detailed dermal papillae in the model.

4.2 The microstructure of skin in three dimensions

A gap exists between the natural geometry and conventional FE models because 2D models assume identical geometry along the depth direction (Fig 4-1b). In contrast, Cauna's observation [12][1] revealed the convex-concave structure of dermal papillae. Additionally, RA-I receptors are located at common apexes of both dermal papillae and the intermediate ridge (Fig 4-1c), and thus, a 3D model with both intermediate ridges and dermal papillae (3D microstructure) is required to investigate their mechanotransduction.

Vodlak [77] developed a full-scale fingertip with a single representative volume of dermal papillae (containing one RA-I receptor) that focused on the anatomical detail of the RA-I receptor and its transduction method. This model is potentially useful in investigating 3D microstructure although modeling the 3D microstructure at the macro-scale is complex and computationally expensive.

This paper presents a small-scale model that includes the 3D microstructure of dermal papillae. The proposed model is validated with a standard line-load method. This is followed by comparing the 3D model with a model with a 2D microstructure to demonstrate how the 3D microstructure affects the SED concentration at mechanoreceptor positions, i.e., at the base of intermediate ridges (SA-I receptor position) and especially at the tips of dermal papillae (RA-I receptor position). The results indicate that the SED is high at the RA-I receptors near the edge of the indenter in dynamic experiments. During vibrating experiments, the response of SED at a single RA-I location increases when the frequency of vibration increases to 80 Hz.

4.3 Methods

4.3.1 FE models

The model was considered as a cut-away cube of a fingertip and contained six fingerprints along with 12 intermediate ridges with exterior measurements as shown in Fig 4-2. The configuration of the limiting ridges is excluded. The model is relatively small, and the fingerprints are arranged evenly. The depth of skin calculated from the surface of the epidermis to the center of bone typically approximately corresponds to 11.55 mm while the convex of the surface is less than 0.121 mm. The difference ratio approximately corresponds to 1.04%, and thus it is reasonable to assume that the surface is flat in this case. This assumption is also supported by anatomical observations [78]. A thin layer of subcutaneous tissue is used as a buffer, and its thickness is determined through a line-load validation as described in the next section. This modeling method reduces the calculation cost while allowing the model to have a sufficient thickness for deformation in three dimensions.

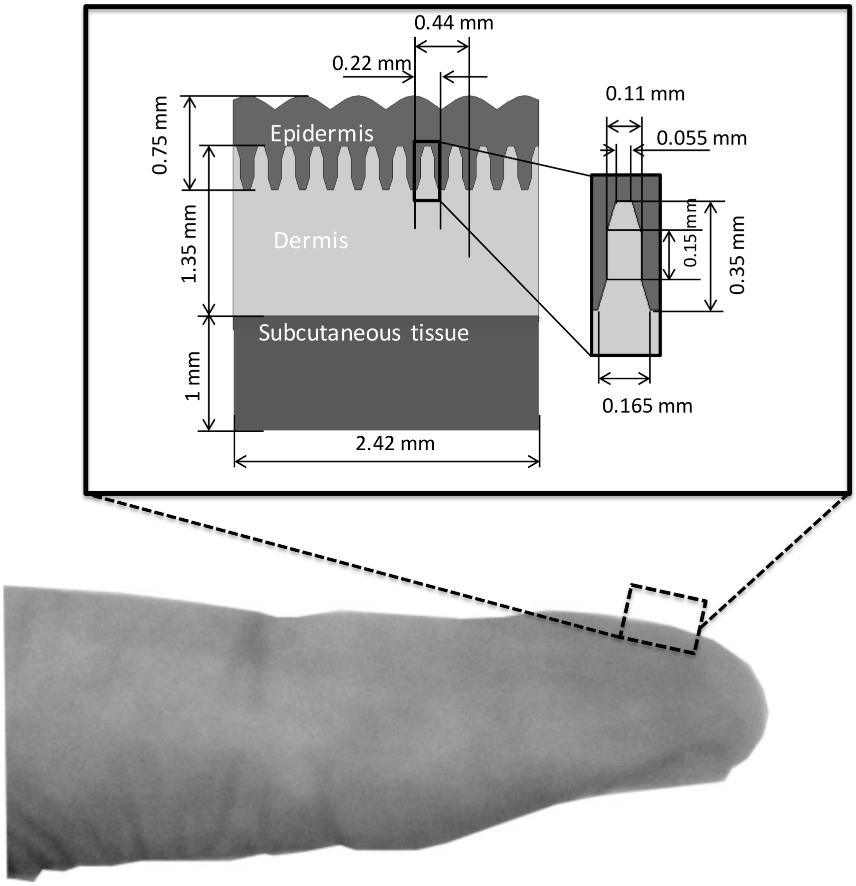

Figure 4-2: A simplified elastic model mimicking a cut-away cube of the human fingertip. Inset: exterior measurements and measurement of a single intermediate ridge.

Two models were created for the simulation, namely 2D and 3D ridged models. The 2D ridged model includes intermediate ridges, which are concave-convex structures with trapezoid apexes. The dermal papillae are considered to possess even geometry (Fig 4-3a). The 3D ridged model includes the same intermediate ridges and the concave-convex dermal papillae along the depth (144 tips in total). The dermal papillae are simplified into trapezoid apexes and bases with the same width as those of the intermediate ridge. The length of dermal papillae is set at 0.15 mm, and this is equivalent to the average length of an RA-I receptor in humans (Fig 4-3b).

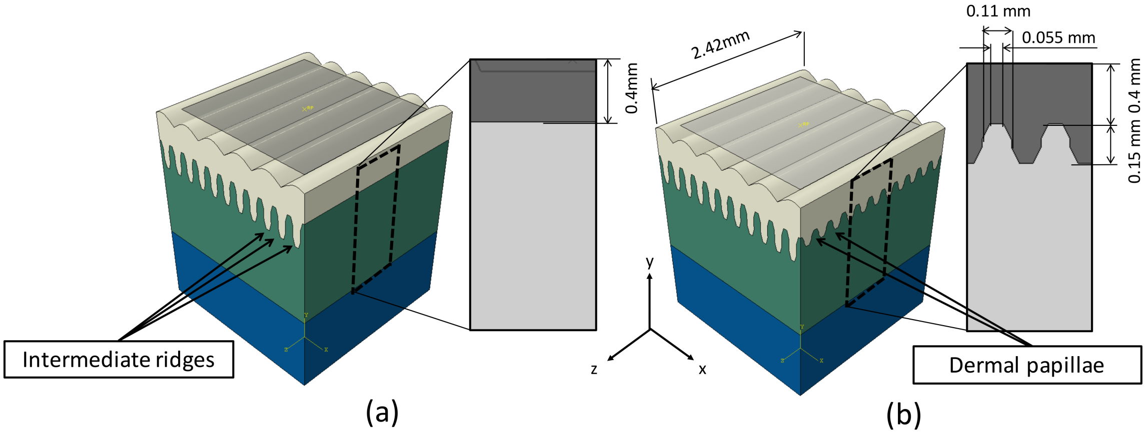

Figure 4-3: Depth configuration of (a) the 2D ridged model and (b) the 3D ridged model. The epidermis, dermis, and subcutaneous layers are shown in white, green, and blue colors, respectively. The gray plane represents an example of a solid indenter ($2 \times 2 mm^2$). The apexes of dermal papillae exhibit the same structure and measurements as those of intermediate ridges.

The models are multi-layered and include the epidermis, dermis, and subcutaneous tissue (Fig 4-2) with elastic properties as adapted from previous studies [32]. The Young's modulus corresponds to 0.136 MPa for the epidermis, 0.08 MPa for the dermis, and 0.034 MPa for the subcutaneous tissue. The Poisson's ratio corresponds to 0.48 for each layer [32] [4] [79]. In this study, we focus on the mechanical response at RA-I location under small displacement loads, and thus the model is assumed as linearly viscoelastic. Sophisticated hyperelastic models [80] are excluded as [81] [2] suggested that a non-linearity model is necessary for large displacement loads. As suggested by [2], the outer most layer is linear elastic and the others are viscoelastic. The total stress is as follows:

$$\sigma(t) = \sigma_0(t) + \int_0^t g(\dot{\tau})\sigma_0(t-\tau)d\tau \tag{4.1}$$

where t denotes time, g(t) denotes the stress relaxation function, and $\sigma_0(t)$ denotes the instantaneous stress. We define g(t) as a two-term Prony series.

$$g(t) = 1 - \sum_{i=1}^{2} g_i(1 - e^{-t/\tau_i}) \tag{4.2}$$

where g_i and τ_i denote the stress relaxation parameters that are obtained by fitting the net force response of the model to the experimental data as adopted from [2]. The fitting program is developed and implemented in Python with the support of the Scipy (v0.19.0) library.

The finite element software ANSYS release 16.0 (ANSYS Co.) is used to mesh and analyze the responses. The mesh uses 20-node solid brick elements for surface-to-surface contact. The coefficient of friction between the models and indenters is assumed as zero due to small indentations. The numbers of nodes and elements in 3D ridged models correspond to 267,156 and 88,482, respectively. The numbers of nodes and elements in 2D ridged models correspond to 114,879 and 34,131, respectively. The differences in numbers are due to the complexity of dermal papillae structures in the 3D ridged model. The experiments are conducted in dynamic conditions. Restraint conditions are assumed based on validation experiments that employ various restrained circumstances.

4.3.2 Viscous parameters calibration for dynamic experiments

We simulate the indentation experiments with a cylindrical indenter as performed in [2]. The indenter is circular with a diameter of 0.5 mm. The indenter is ramped up to 0.2 mm (0.5 mm/s) and held for 3 s and then completely retracted. We calculate the contact force at the surface of the fingerprints as a function of time. Fig 4-4a describes the displacement history of indenter, and Fig 4-4b shows the predicted contact force when compared with the experimental data. A difference in magnitude is expected due to the lack of rigid fixed parts such as bones and nails. Fig 4-4c shows that the decay of normalized force in our model is similar to that observed by [2].

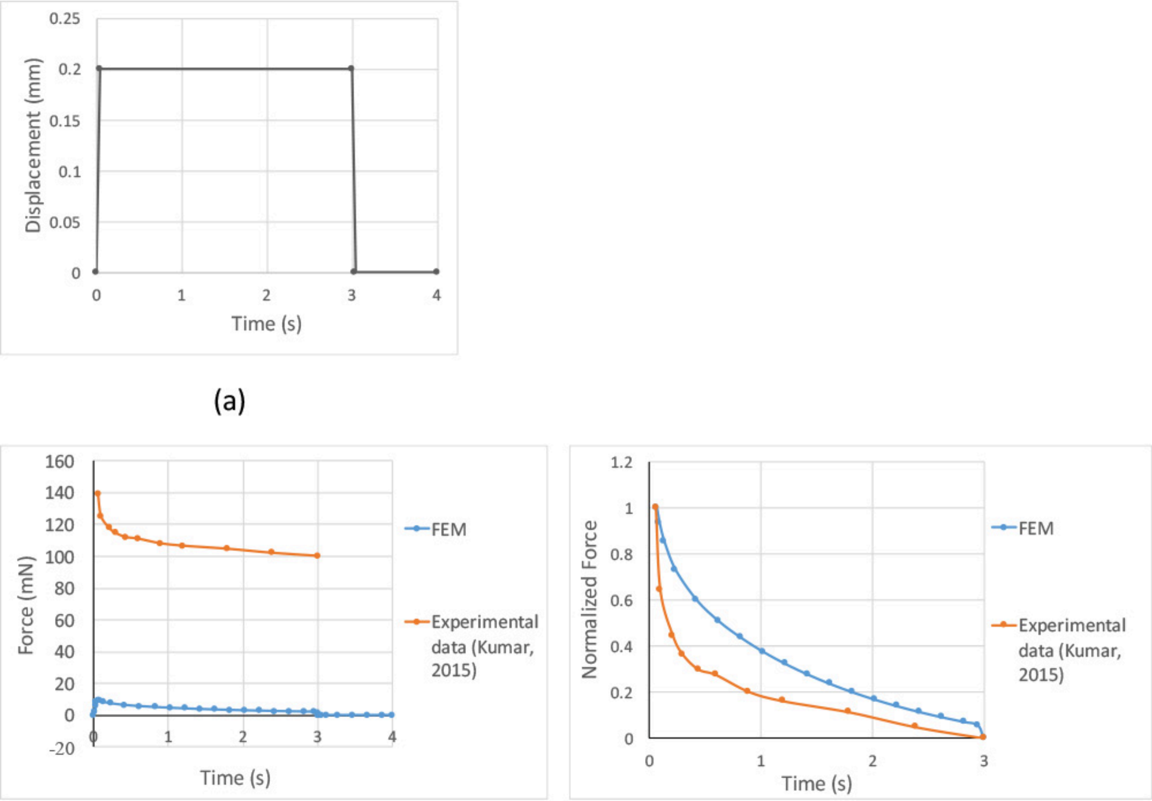

(b) (c)

Figure 4-4: Viscous parameters calibration. (a) The displacement history of an indenter. (b) Profiles of the absolute contact force from the model and experimental data from [2]. (c) Profiles of normalized contact force in relaxation periods showing a good match between the model results and experimental data.

4.3.3 Experiments

Model validation

The displacement at the surface of model (in response to 50 μm line load indenter) is compared to experimental data from [5] to validate the mechanical response of the model. The line-load indenter results in a displacement of 1 mm that is perpendicular from the surface of the models (at the rate of 1 mm/s) and is held for 2 s. The surface deflection is computed at t=2 s to allow the model to reach its stable condition. Three restraint conditions are tested to determine the boundary condition that best

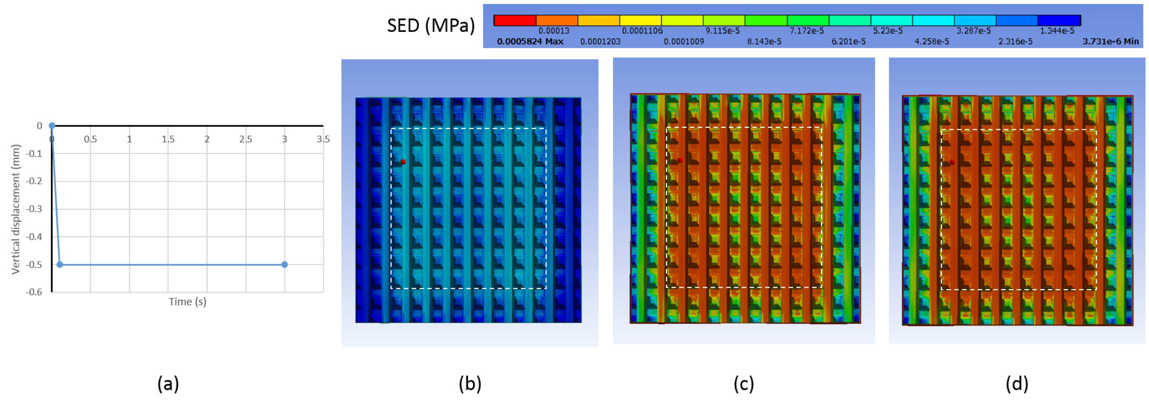

Figure 4-5: Top view of dermis part of the 3D ridged model during ramp-and-hold experiment. (a) Displacement profile of solid bar indenter. Distribution of SED at RA-I locations at (b) t=0.01 s, (c) t=0.1 s, and (d)t=2 s. The white square is the range of indenter.

approximates the observed displacement behavior, namely full-restrained (bottom and surrounds), bottom-faces-restrained, and bottom-edges-restrained conditions (Fig 4-6a). The models used for the three boundary conditions are denoted as 1x020s, 1x020f, and 1x020e.

Another boundary test focuses on the thickness of the subcutaneous layer. The thickness of the subcutaneous layer varies in range of 0.2 mm, 0.4 mm, 0.6 mm, 0.7 mm, 0.8 mm, and 1 mm and the six conditions are as denoted 1x020e, 1x040e, 1x060e, 1x070e, 1x080e, and 1x100e, respectively). All the models were bottom-edges-restrained.

Ramp-and-hold experiments

In order to investigate the effect of a 3D microstructure, a $2.0\times2.0\ mm^2$ bar provides displacement to a depth of 0.5 mm from the model surface at the rate of 5 mm/s and is held for 2 s (Fig. 4-5). The displayed time point is the first time that the indenter reaches its deepest position (t=0.1 s).

Two 3D distributions of stress are plotted to address the effect in the population. The SED at the position of RA-I receptor was measured at the tips of intermediate ridges (in the 2D ridged model) and the common tips of intermediate ridges and dermal papillae (in the 3D ridged model). The strain rate is constant during the ramp phase, and thus the stress-strain curves are non-linear. For the purpose of convenience, the concept of equivalent strain energy density is used [82]. The convex-concave shape of dermal papillae is considered, and the stress-strain behavior at their tips is similar to the elastic-plastic behavior at a notch tip. The Glinka's concept relates equivalent strain energy density for an elastic fictitious material as well the real elastic-plastic material during a low strain. Hence, the SED is estimated as follows

$$U = \int \sigma d\epsilon \approx \frac{1}{2}\sigma^e \epsilon^e \tag{4.3}$$

where σ^e denotes equivalent stress and ϵ^e denotes equivalent strain. The equivalent stress and equivalent strain is related to the principal stresses and strains as given by the following equations

$$\sigma^e = [\frac{(\sigma_1 - \sigma_2)^2 + (\sigma_2 - \sigma_3)^2 + (\sigma_3 - \sigma_1)^2}{2}]^{\frac{1}{2}} \tag{4.4}$$

$$\epsilon^e = \frac{1}{1+\nu}(\frac{1}{2}[(\epsilon_1 - \epsilon_2)^2 + (\epsilon_2 - \epsilon_3)^2 + (\epsilon_3 - \epsilon_1)^2])^{\frac{1}{2}} \tag{4.5}$$

where ν denotes the material Poisson's ratio.

The SED distribution at 10 specific x-axis-crossed surfaces, namely eight in-range and two out-of-range from the indenter for comparison, are recorded and then superimposed.

In order to examine whether the 3D microstructure can help in discerning a similar indenter, we additionally analyze the normalized SED distribution of the following three indenters: a gap indenter (comprising two 0.5×2 mm^2 indenters with a 1.0×2.0 mm^2 gap between inside edges), a 90-degree-rotated gap indenter, and a solid circle indenter (with a diameter of 2 mm). The normalized SED (ε_i) at the i^{th} sample of data is as follows

$$\varepsilon_i = \frac{A_i - min(A)}{max(A) - min(A)} \tag{4.6}$$

where A represents the dataset of SED, and A_i denotes the absolute value of SED at the i^{th} sample. The normalized SED is contoured into a 10 × 10 table with each cell relating to a specific tip of dermal papillae (i.e., 100 tips in total). Only "hotspots" that correspond to the positions that fall into the right side of the scale bar are plotted; i.e., the threshold corresponds to 0.6. The size is adjusted for better visualization of the distribution as opposed to considering the absolute value.

Vibration experiments

The RA-I is sensitive to stimulus in range of 20 to 50 Hz, and thus indentation experiments with four vibrating stimuli (with different frequencies corresponding to 20 Hz, 30 Hz, 50 Hz, and 80 Hz) are conducted. The indenter is a $2 \times 2\ mm^2$ plane. The amplitude is maintained at 0.5 mm. Previous studies [83] indicated the highest spike rates of RA-I when indenters reached their deepest position. Thus, the frequency-dependent SED response is plotted at a single RA-I near the edge of the indenter at the following time point(e.g., t=0.005 s for 50 Hz stimuli).

4.4 Results

4.4.1 Model validation results

Fig 4-6 shows the predicted surface deflection of skin fitted relative to the experimental data for a human finger. Only half of the profiles are shown due to reasons of symmetry. The maximum displacement of the line-load in the cases of the full-restrained and bottom-face-restrained models is as low as 0.25 mm. The model with the bottom-edge-restrained condition better fits the experimental data as shown in Fig 4-6b.

The thickness of the subcutaneous layer appears to strongly affect the result of line-load validation. The models with a thickness of the subcutaneous layer ranging from 0.6 mm to 1 mm well fit both the experimental data [5] and the linear-elastic model from [4] as shown in Fig 4-6c. Each set of 2D and 3D ridged models were treated equally, and thus, the elastic characteristics are similar in both conditions. The 1x100e model (that includes original dimensions with a 1-mm-thick subcutaneous layer; bottom-edge restrained) fit experimental data [5] the most. Hence, the 1x100e

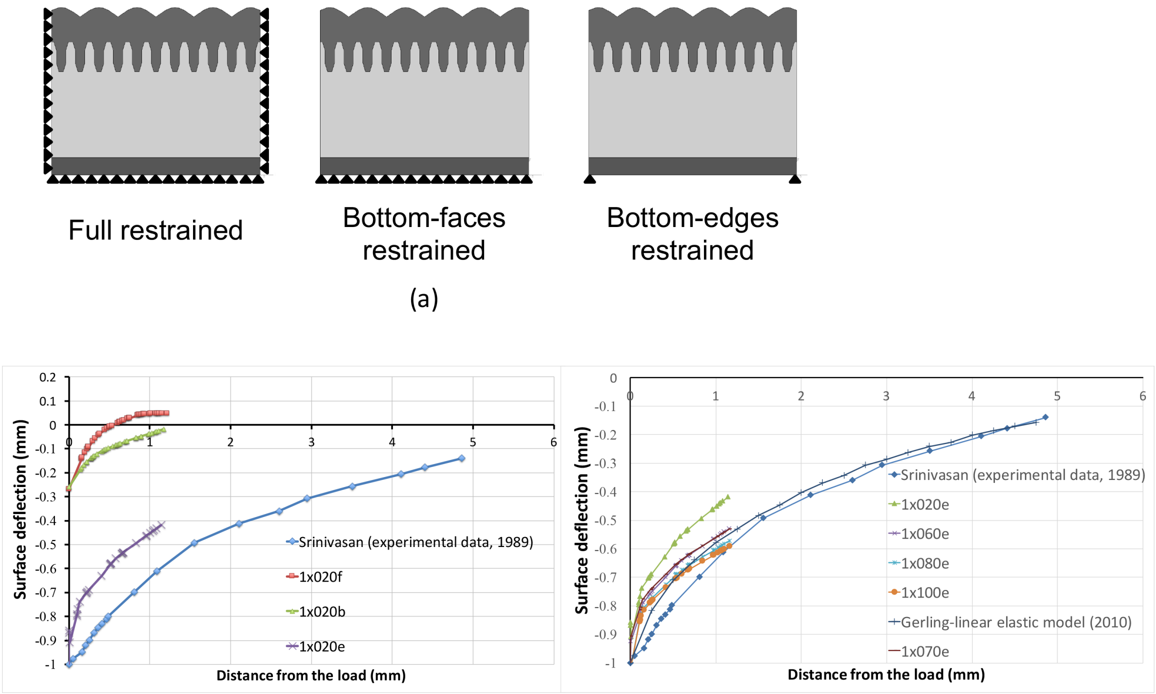

(a)

(b)

(c)

Figure 4-6: Line load validation test, 50 micrometers. (a) Illustration of three tested restraint conditions. Black triangles represent fixed boundary conditions (an assumption). (b) Surface deflection of the models under each restraint condition when compared with experimental data from Srinivasan et al. (1989). (c) Surface deflection of the models with different thicknesses of cutaneous tissue.

model was used in ramp-and-hold experiments and vibration experiments.

4.4.2 Ramp-and-hold experiment results

Fig 4-7 illustrates the SED distribution along the z-axis of an intermediate ridge in the case of the bar indenter. The centers of both models only contained the bases of the intermediate ridges, and thus, the observed surface is shifted along the x-axis to the cross section where the SED is highest. The SED is high at the corners of indenters in the 2D ridged model (Fig 4-7a) although it diffuses separately into the dermal papillae in the 3D ridged model (Fig 4-7b). A high SED is observed at each tip of the dermal papillae.

The 3D distribution of SED at the tips of dermal papillae after pressing by the solid bar indenter is shown in Fig 4-8. The vertical axis presents the magnitude of

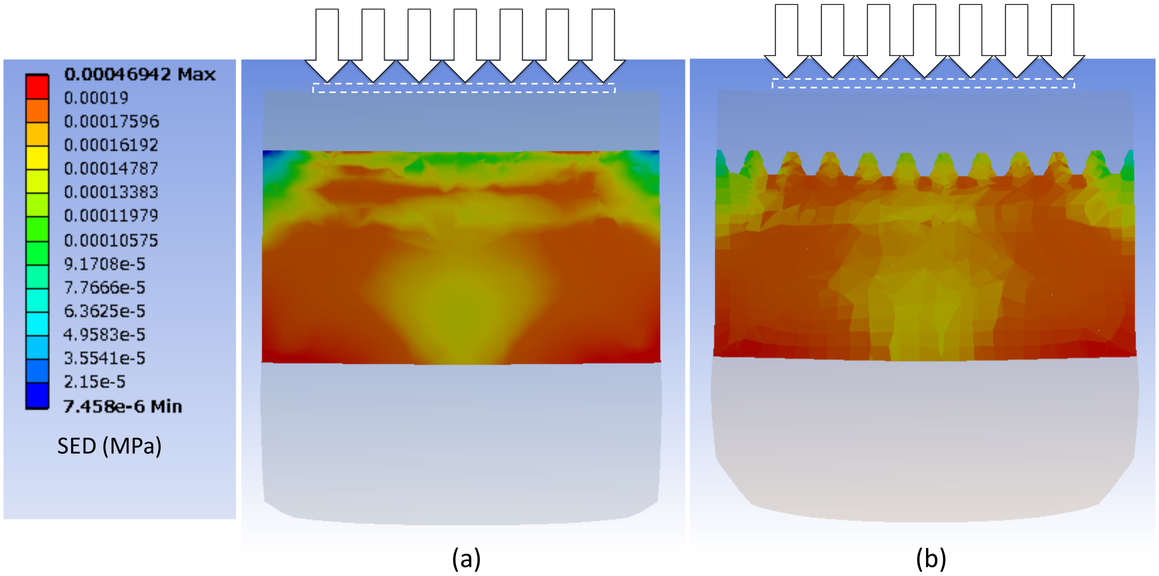

Figure 4-7: SED distributions along the z-axis of an intermediate ridge. (a) the 2D ridged model and (b) the 3D ridged model. The white square denotes the range of the indenter. Only the dermis is shown. The maximum SED of the scale bar at the left is set at 0.00019 MPa.

SED, the horizontal axis presents the distance along the z-axis from the center, and the depth axis presents the distance along the x-axis from the center. The peak value of SED in the 3D ridged model exceeds that in 2D ridged model. A valley is observed at the center of the apex and indicates an interchange zone (peak-valley-peak) in both models. The contour of the normalized SED in the case of solid bar indenter reveals that the interchange zone of the 3D ridged model along the z-direction is more significant than that of the 2D ridged model (Fig 4-9). Along the x-direction, the interchange zone is equally noticeable in the two models.

A summary of the normalized dataset is shown in Fig 4-9. In the 2D ridged model, the SED is mostly high at the four corners of the indenters (for example, solid bar indenter and 90-degree-rotated gap indenter) while it mostly high at the edges of the indenters (and especially along the z-axis) in the 3D ridged model. The 3D ridged model produces distributions of the normalized SED at the RA-I receptor location that differentiate the indenters. Furthermore, the 2D ridged model shows little difference between the normalized SED distributions of the solid bar indenter and gap indenter. It is evident that the 3D microstructure significantly influences

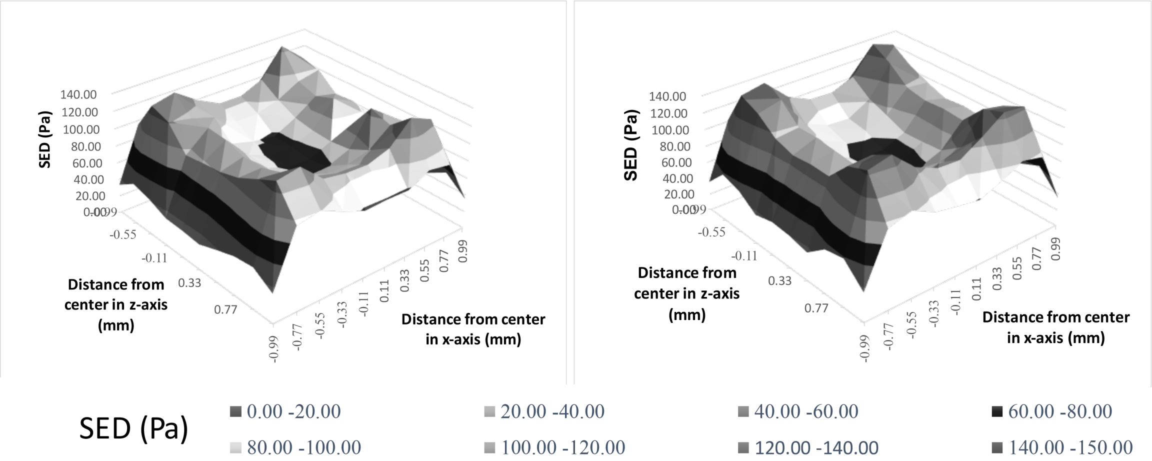

(a) (b)

Figure 4-8: 3D distribution of SED at the tips of dermal papillae underlying the indenter. (a) the 2D ridged model and (b) the 3D ridged model.

encoding spatial differences among the indenters.

4.4.3 Vibration experiment results

Fig 4-10b, c, d show the SED distribution at a population of RA-I location during vibration by 50 Hz stimuli. The displayed time-points correspond to 0.001 s, 0.005 s, and 0.01 s. The observed model is a 3D ridged model. The localizing effect in which the SED is high near the edges of the indenter is observed at t=0.005 s. The localizing effect is unlikely to be observed at the other time-points,.

In order to examine the change of SED when the frequency increases, the SED at a RA-I location (with the maximum SED value) is plotted and compared with the following position in the 2D ridged model (Fig 4-11). In the 3D ridged model, the SED increases when the frequency increases to 80 Hz while it remains constant in the 2D ridged model.

4.5 Discussion

Previous studies showed the effect of microstructure on stress/strain behavior at the position of mechanoreceptors (SA-I and RA-I) where the microstructure amplifies

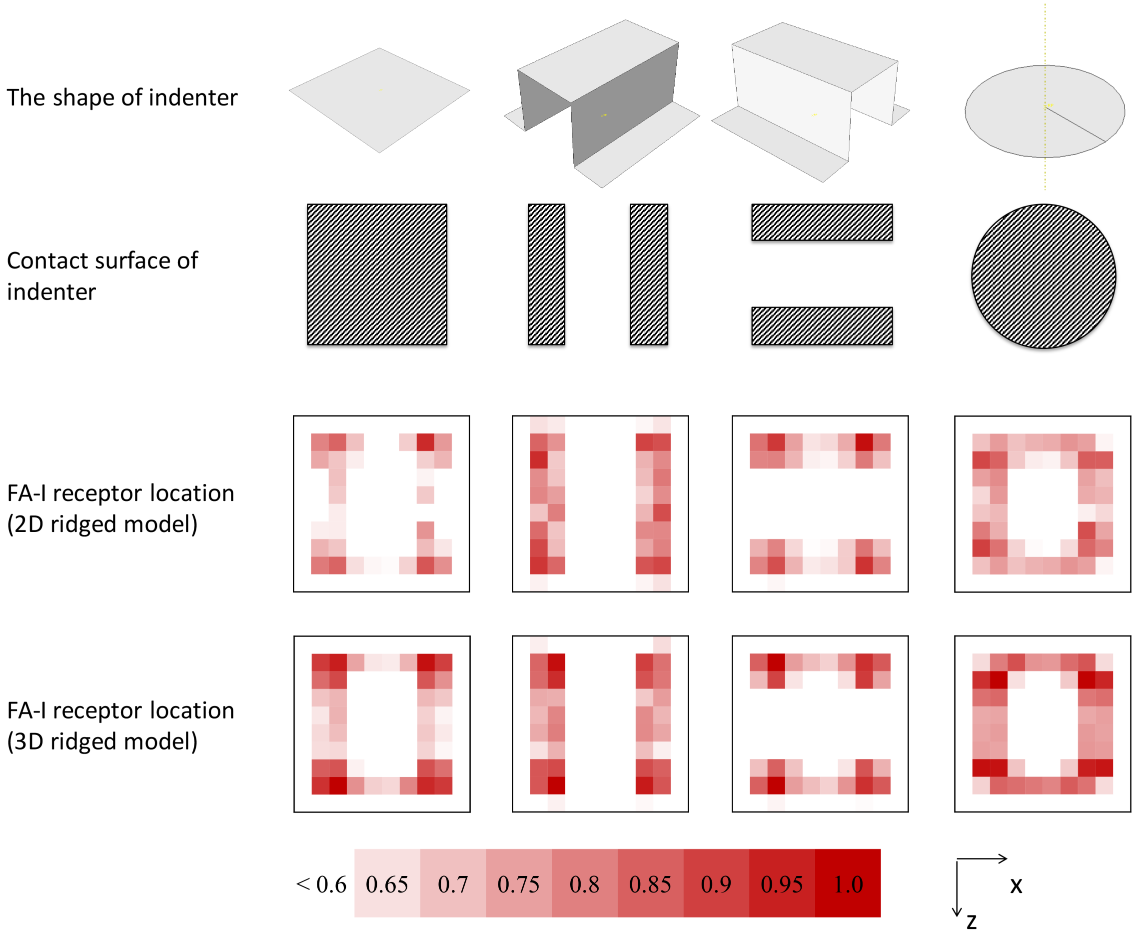

Figure 4-9: Summary of the normalized SED distribution at the SA-I receptor location and RA-I receptor location, corresponding to the indenter. The indenters are as follows (from left to right): a solid bar indenter, a gap indenter, a 90-degree-rotated gap indenter, and a solid circle indenter. The scale bar shows a gradient from white to red as the normalized SED increases from 0.6 to 1.0. Values under 0.6 are not plotted.

the SED concentration at the SA-I receptor's location. However, most studies were conducted in two dimensions since they lack the depth configuration of dermal papillae and overlooked the effect of the RA-I receptor positions. The present study involved proposing and developing a model that presents the 3D microstructure of skin in significant detail (i.e., a 3D ridged model). The boundary conditions were determined through a validation experiment with a standard line load method (Fig 4-6). The viscous parameters were determined by fitting the normalized contact force on the circular indenter to the experimental data reported by [2]. The approach reduces the

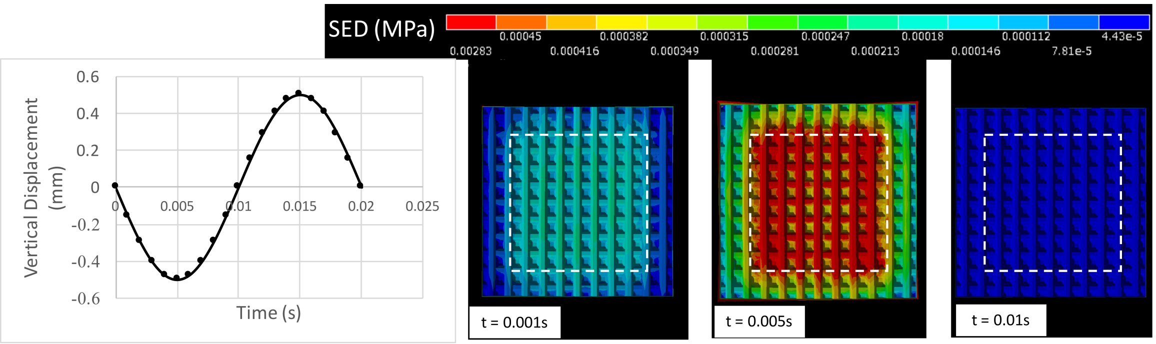

(a) (b) (c) (d)

Figure 4-10: Top view of the dermis part of the 3D ridged model during vibration by a 50-Hz stimuli. (a) Displacement profile of a 50 Hz vibratory indenter. Distribution of SED at RA-I locations at (b) t=0.001 s, (c) t=0.005 s, and (d)t=0.1 s. The white square depicts the range of the indenter.

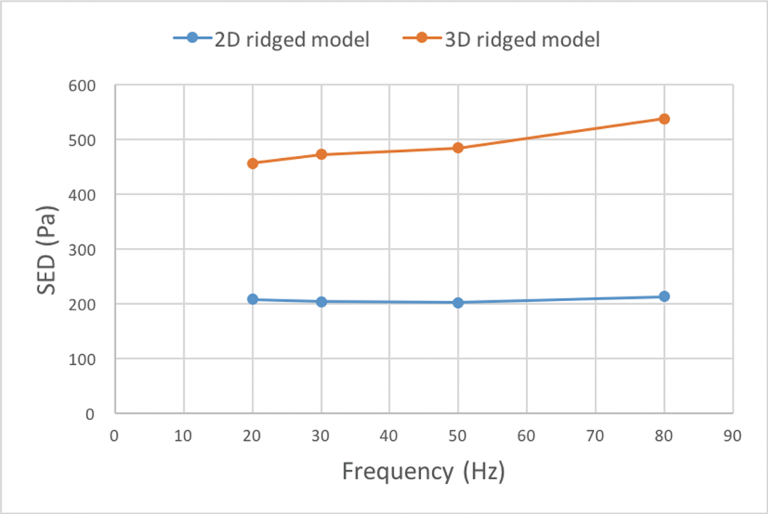

Figure 4-11: SED response at a RA-I location as a function of frequency, and a comparison of the 3D model and the 2D model.

calculation cost while ensuring that the performance of the model is comparable to that of other models. The limitations of the model will be discussed in the final part of this section.

Our main finding indicates that the 3D microstructure appears to modify the distribution of SED at RA-I receptor's positions such that it helps in discerning the spatial configuration of similar indenters (Fig 4-9). This finding agrees and interprets the conclusion of a recent study by Harih et al. [84] in which the 2D and 3D fingertip

FE models were justified during static contact simulation. Although the results of the 2D and 3D model in [84] were similar (possibly due to the lack of microstructure), the 3D model provides additional insights into the third dimension. The results suggest that the 3D microstructure provides focalizing effects and especially localizing effects as described below.

4.5.1 The diffusion of SED and the focalizing effect

The focalizing effect describes the trend of SED concentration at the tips of dermal papillae (RA-I receptor's positions). The effect occurs when the contact surface exhibits uneven geometry and the stiffness of the epidermis and dermis are significantly different. Gerling [85] demonstrated the lensing effect of ridged geometry in a 2D model of a microstructure and concluded that stress is more concentrated at the bases of intermediate ridges. In the 3D model of the microstructure, we confirmed a similar effect given that a high concentration of SED was present. at the tips of the dermal papillae in Fig 4-7.

4.5.2 Localizing effect of 3D microstructure and its potential roles in spatial discrimination

The localizing effect describes the peaks of the 3D distribution of SED located at the tips of dermal papillae near the edges of the indenter (Fig 4-8). The contrast between these positions and others produced a specific pattern that reflects the shape and the size of the indenter (Fig 4-9). The localizing effect was confirmed in both ramp-and-hold experiments (Fig 4-9 and Fig 4-5) and vibration experiments (Fig 4-10) at the moment when the indenters reached their deepest positions.

The 3D ridged model appears to be sensitive to the edges of the indenter with a valley of SED values at the center. In the case of the solid bar indenter, the interchange zone in the x-axis (peak–valley–peak) is more noticeable than that in the z-axis (Fig 4-9). This behavior may be related to the presence of fingerprints along the x-axis given that the fingerprints are believed to affect the stress/strain concentration at the dermal papillae as shown in [32].

Interestingly, the normalized SED distributions at the RA-I receptor location were sensitive to the edges of indenters in most experiments (see Fig 4-9). This finding does not contradict the hypothesis that the SA-I receptors are more sensitive than RA-I receptors in terms of shape discrimination (for details, see [29, 7]). However, it indicates that the mechanical response at RA-I receptor location might provide complementary information for better discrimination under dynamic conditions.

4.5.3 Effect of 3D microstructure in vibratory conditions

In the 3D model of the microstructure, the SED response at a RA-I location increased when the vibratory frequency increased from 20 Hz to 80 Hz (Fig 4-11), irrespective of the widely-known maximum sensitive frequency of the RA-I receptor (50 Hz). The increase is understandable since the viscous force is proportional to velocity. In this study, the amplitude was kept constant in all experiments, and thus the higher frequency stimulus is displaced at a higher velocity.

Interestingly, the SED response at a RA-I location in the 2D ridged model remained unchanged (Fig 4-11). Evidently, either the increase was extremely small in the 2D ridged model or the energy was further concentrated at other positions, e.g. SA-I locations. Meanwhile, in the 3D ridged model, the increase in SED response at a RA-I location was high due to the focalizing effect. This result indicates the requirement for a 3D model of microstructure for RA-I related analysis in vibratory conditions.

An electrophysiological report published by Bensmaia [3] showed that the spike rates also gradually increased from 20 Hz to 80 Hz, and this was similar to the SED behavior observed in our study (Fig 4-12). This result is in agreement with the results obtained by previous studies that suggested a relationship between the dynamic spike rate and local SED at a mechanoreceptor's location [2] (in this case, this is at the RA-I location).

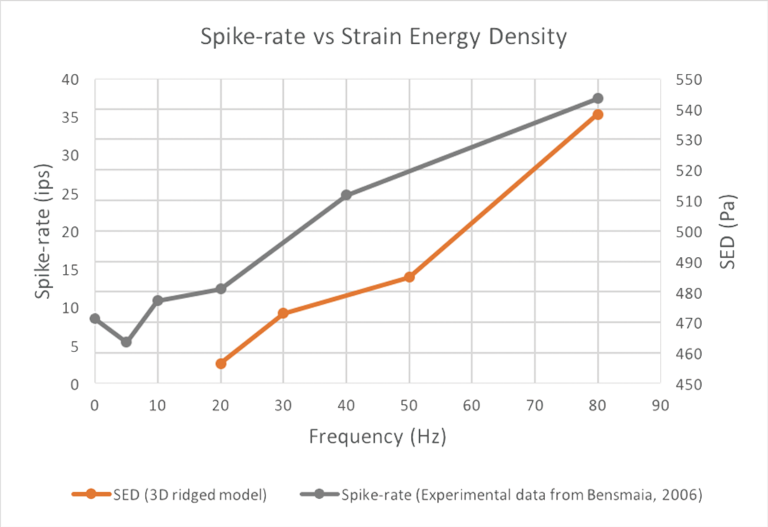

Figure 4-12: Comparison of 3D model and the mean spike rates of RA-I, adapted from [3].

4.5.4 The potential use of 3D microstructure in tactile sensor design

In terms of tactile sensor design, the elastic cover is highly essential to protect the sensor from being damaged by external forces [86]. However, Shimojo [87] demonstrated that the elastic cover significantly reduced the spatial resolution of the sensor even if the cover thickness is only 0.2 mm. Various studies mimicked the natural geometry of human finger microstructure in sensor design to improve tactile sensing ability while retaining protection such as studies that indicated that artificial epidermal ridges enhanced strain gage sensitivity by 1.8 times when compared with tactile sensors without ridges [88] or enhanced tactile shape discrimination [89, 90]. An optical tactile sensor developed by Chorley et al. [91] with an array of identical urethane pins as artificial dermal papillae were capable of encoding edge information.

Here, we propose the potential use of a 3D microstructure in tactile sensor design. Given the assumption that the sensing elements respond equally, placing the same at different positions of 3D microstructure allows us to achieve different effects intentionally. The positions at the tips of dermal papillae enhance the spatial discrimination of the tactile sensor (our finding) while the positions at the bases of the intermediate ridges enhance the sensitivity (as suggested in [4]). The contour of the 3D ridged model in Fig 4-9 implies the tactile image obtained by embedding sensing elements at the tips of dermal papillae under the following circumstances.

4.5.5 The limitations of proposed model and future works

The limitation of the model is that the model is small, and this restricts the size of the indenters. The current model cannot be used to show the response at sides (left-right) of the fingertip. It is necessary to develop a large-scale model with respect to the complexity and computational cost to facilitate comparisons with physiological or electrophysiological experiments. Physiological or electrophysiological experiments are usually conducted with indenters larger than 2 mm. In this study, the neuronal responses of RA-I mechanoreceptors were not examined due to the lack of a neuronal model. Additionally, the neuronal response of RA-I mechanoreceptor is suggested as a combination of population activities [3, 17]. It is unknown as to precisely how the RA-I mechanoreceptor modifies responses during the combination. Hence, the determination of the manner in which the RA-I mechanoreceptor processes the population mechanical responses into neural responses is an interesting challenge for future work. To investigate the neuronal responses of RA-I mechanoreceptors, one could use a transduction function to transform the SED into neural current. The transduction function was assumed as a sigmoidal stimulus-current curves in [92], and as a two linear function in [30]. Then the spike times could be obtained by using the leaky integrate-and-fire model.

Chapter 5

Analysis of the transduction layer and synthetic sub-model for investigating the RA-I afferent response

Rapid adapting type-I (RA-I) receptor is believed to be responsible for the detection of stimuli that produce minute skin motion (flutter, slip, microgeometric surface features). The neurophysiological experiments raise a question about why the RA-I afferent (innervated into RA-I receptor) fails to represents the stimulus with the width less than 3 mm and why their response is anisotropy. It is unclear whether the skin's mechanics or the specific afferent branching of mechanoreceptors themselves are accounted for these phenomena. The present work seeks an interpretation of the neurophysiological phenomena, using a biomechanical FE model with a transduction sub-layer and synthetic sub-model for afferent current. The predicted afferent current matched well with the neural recordings in previous reports. This result suggests a major role of afferent branching in regard to the neurophysiological phenomena.

5.1 Introduction

There has been a number of publications using solid mechanics technique to study the mechanics of touch. Srinivasan [33], Maeno [32], Wu [80], Gerling [4] have established a popular use of the 2D finite-element (FE) model of cross-sectioned fingertip, involving with fingerprint ridges and/or dermal papillae. In these works, the distribution of stress and strain in the skin's tissues are computed and compared to the in vivo neural recordings. So far, the focus has been on SA-I receptor (with Merkel cells as endings organ), a little attention has been given to the RA-I receptors. The 2D model assumes an unrealistic identical geometry along the depth direction, thus it is insufficient for investigating the population response of RA-I receptors. Some recent 3D models [77, 93] attempted to implement the realistic morphology of Meissner corpuscle (ending organ of RA-I afferents). Because of the extreme complexity of Meissner corpuscle, i.e. the spirals shape axons sandwiched between lamella cells (for details, see [22]), neither the population response nor the afferent branching were examined.

The present work seeks an interpretation of the tactile neurophysiological phenomena, using a biomechanical FE model. We have investigated a 3D FE model of skin for the analysis of mechanical response [94]. This work presents the population response of RA-I by using the 3D FE model. Three dependent variables, i.e. strain energy density (SED), receptor current, and afferent current are used to predicts the population response of RA-I. In this paper, we describes design of transduction sublayer for transforming SED response into receptor current and a synthetic model for afferent current. Although the relative contribution of stress, strain to RA-I receptor current is not fully known, SED at RA-I receptor position was used as a proxy measure. The predicted afferent current which was the summation of receptor current in longitudinal sections, showed a good fit to neural recordings in regard to the neurophysiological phenomena mentioned above.

5.2 Method

5.2.1 FE-Model of skin mechanics

A 3D Finite Element model of skin was used, including three homogeneous layers, i.e. epidermis, dermis, and subcutaneous layer (Fig. 5-1). The model was developed previously in [94]. Two microstructures, fingerprint and dermal papillae (the middle region between epidermis and dermis) were included. The dermal papillae were developed based on the description of Cauna et al.[1] with uneven structure in both z-axis and x-axis. In nature, the RA-I receptors are positioned within the apexes of dermal papillae. Therefore, this configuration allows us to precisely locate the RA-I-population, and examine their response in three dimensions. The dimensions of components like fingerprints and thickness of each layers are similar to Maeno et al.[32], except the thickness of subcutaneous was 1 mm. In front view, the thickness of the epidermis and the dermis is 0.75 mm and 1.35 mm, respectively. The interval between the protuberances in the fingerprints is 0.44 mm and the interval between the protuberances in the dermal papillae is 0.22 mm. The length of dermal papillae tips along x-axis is 2-times longer than those along z-axis in respect to their natural dimensions.

Table 5.1 shows the assigned material properties. The model is linear elastic.

Table 5.1: Material properties of skin's components

	Epidermis	Dermis	Subcutaneous layer
Young modulus (MPa)	0.136	0.08	0.034
Possion ratio	0.48	0.48	0.48

All analyses were performed using Abaqus Standard (version 6.15) software in implicit mode. The ten-node tetrahedral elements (C3D10) were used for surface-to-surface contact. The bottom edges of subcutaneous layer were restrained while the other surfaces (i.e, the surrounding surfaces, the top surfaces of the epidermis) were

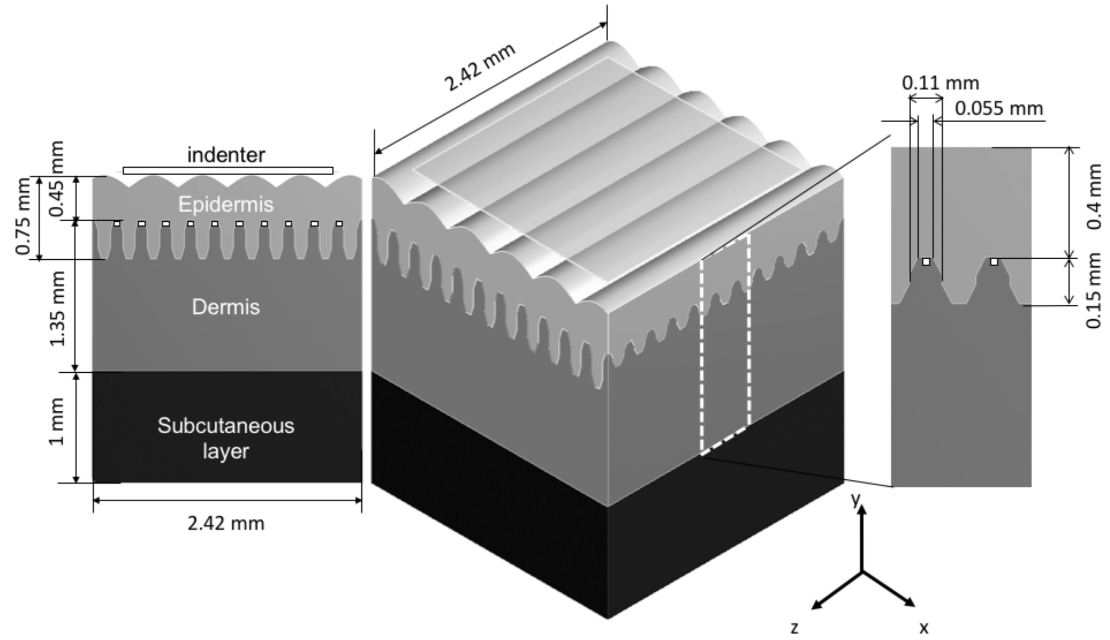

Figure 5-1: Finite Element model of skin. The upper plane illustrates the position and the shape of indenters. The tiny white squares at the right indicates the positions of RA-I receptor.

unrestrained. This restraint condition allows the model to deform freely as the real skin. Since the indentation was small, the coefficient of friction between the skin and indenters was assumed as zero. The result of the validation with line-load method is described in section 3.1. The total nodes and elements were 207,154 and 131,769, respectively.

The model also included a transduction sub-layer which transforms the SED at RA receptor into receptor current (I). The stimulus-current curves at receptors such as hair cells and pain receptors have been shown to be sigmoidal in previous works [95, 96]. Therefore, this work employs a sigmoidal function (Eq.5.1). α, γ, λ are the model parameters obtained through model fitting when the difference between model predictions and in vivo firing rates is minimized.

$$I(SED) = \alpha \frac{1}{1 + \mathrm{e}^{\gamma(\lambda - SED)}} \tag{5.1}$$

The model fitting at this layer is achieved through response surface methodology

(RSM) [97] as in [92]. The RSM was designed with three parameters (α, γ, λ) and two levels (coded values: 1 and -1) for each. This yielded 8 factorial runs and one supplement run where all parameters take the coded value 0, in each iteration. The RSM process repeated until little or no decrease in sum of squared deviations (ssd) between predicted response and observed response (total 3 iterations). Both predicted response and observed response were normalized beforehand (Eq. 5.6). The RSM processing was developed and conducted in Python with support of PyDOE and Scikit-Learn libraries.

One iteration of RSM process consists of five subsequent steps. First, the model parameters are coded into χ_k (for $k = \alpha, \gamma, \lambda$) by Eq. 5.2.

$$\chi_k = \frac{\xi_k - \xi_{kbase}}{\Delta\xi_k} \tag{5.2}$$

where $\Delta\xi_k$ are code increments, ξ_{kbase} are start value of parameters. As suggested in [92], the code increments were set at 5% of the associated ξ_{kbase}. The start values of parameters and code increments were estimated initially through trial and error (Table 5.2). In the subsequent RSM iterations, they are the values that minimized the *ssd* in previous iteration.

In the second step, the coded parameters χ_k are varied in each factorial run. The model parameters ξ_k are calculated for each coded parameters then the receptors current at each locations is obtained by Eq.5.1. The *ssd* between each dataset of receptors current and experimental data is calculated.

In the third step, first order approximation of the relationship between the coded parameters is obtained by linear regression, given as Eq.5.3.

$$ssd \approx \beta_0 + \beta_\alpha \chi_\alpha + \beta_\gamma \chi_\gamma + \beta_\lambda \chi_\lambda \tag{5.3}$$

In the fourth step, the change in the coded variable, $\Delta\chi_k$ is calculated to most

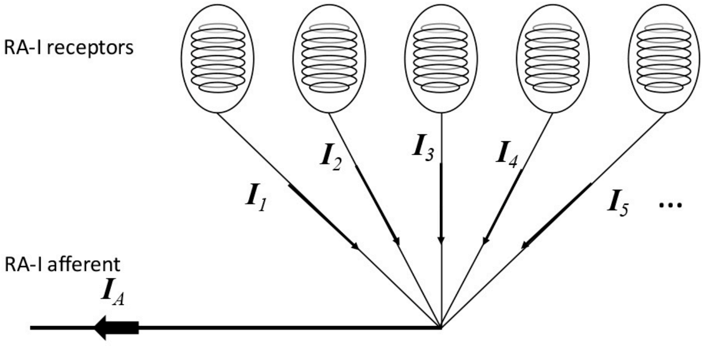

Figure 5-2: Illustration of synthetic model

significantly decrease the *ssd* as follows

$$\Delta\chi_k = \frac{-\beta_k}{|\beta_{max}|} \tag{5.4}$$

where β_k are the regression coefficients for each coded parameter in Eq. (3) and β_{max} is the regression coefficient that has the greatest absolute value. Then the new coded variable χ_k is calculated by adding the $\Delta\chi_k$ to the old coded χ_k.

In the fifth step, the model parameters are recalculated with the new coded variable χ_k. The calculation of the model parameters repeats until *ssd* no longer decreases. After this step, the RSM process repeats.

5.2.2 Synthetic model of RA's population responses

The idea of integration model for RA's population responses is based on the fact that there are small number of afferent fiber in fingertips connecting to a huge number of receptors. Previous works in neurology show the density of RA-I receptor ranges from 12 to 38 receptors/mm^2, while the number of associated afferents has been estimated at 140 afferents/cm^2 in human fingertip (for details, see [24, 17]). A quick calculation gives that one afferent may be in charge of 9-17 receptors. It is reasonable to think the afferent current is basically a combination of its related receptor currents.

Since each RA receptor may produce a different receptor current, this work considers them components in a parallel circuit (Fig. 5-2). Therefore, the output (I_A-Afferent current) of each afferent would be a summation of these receptor currents (Eq.5.1) in one single longitudinal section or one single cross-section (to fingerprint). This work examines which combination approach would yield a better fit to experimental data.

$$I_A = \sum_{i=1}^{n} I_i \tag{5.5}$$

Table 5.2 gives the final model parameters α, γ, λ of transduction sub-layer, relevant to each combination approach.

Table 5.2: The transduction sub-layer parameters

	α (mA)	γ (Pa^{-1})	λ (Pa)	ssd
Start (first iteration)	2.46E-05	4.6E-03	300	0.70
Longitudinal sections combination	9.29E-04	2.95E-02	-705	0.24
Cross-sections combination	2.21E-05	9.66E-03	209	0.45

5.2.3 Analyses

Validation analyses

To verify the usability of the model in this study, a series of preliminary analyses was conducted. First, the elastic behavior of the model was validated by comparing the surface deflection with experimental data from Srinivasan [5] when penetrated by a rigid line.

The second validation involves with a 2×2 mm^2 plane indented into skin surface to the depth of 1 mm. The normalized strain energy density (SED) at SA-I mechanoreceptor position were fitted and compared to neurophysiological recording ([35]). The normalized variable ε_i over i samples (i.e. RA-I receptor locations) was given by:

$$\varepsilon_i = \frac{A_i - min(A_i)}{max(A_i) - min(A_i)} \tag{5.6}$$

where A_i is the dataset of absolute value of SED at the location of ith RA-I receptor.

The relationship between SED and experimentally recorded response are assumed linear as in [6, 4]. The Goodness of fit (R^2) are given by Eq.5.7 where the difference between the predicted response (e_i) and the reported neurophysiological response (d_i) [6] at the location of ith RA-I receptor is minimized.

$$R^2 = 1 - \frac{\sum(d_i - e_i)^2}{\sum d_i^2} \tag{5.7}$$

Note that the SED at SA-I position were used because they are common in this type of validation. The main analysis did not concern with SA-I responses.

Mechanical response of RA population to various size of indentation

The main analysis consisted of a series of square indenter (width varies from 0.44, 0.66, 0.88, 1.1, 1.32 mm) and examined in two steps. First, the indenters ramped vertically to the skin surface (to the depth of 0.5 mm). The analysis time was 0.1s for each. The time-dependence of the deformation was not shown in this paper. We focus on the response at the very moment when the indenter reached the prescribed displacement because the SED was highest at that moment throughout the indentation process.

In the next step, the SED values are collected at RA-I receptor positions. We plot the contour of SED values to observe their distribution in three-dimensions.

Synthetic model analysis

The synthetic analysis was conducted under two approach, i.e, longitudinal sections combination and cross-sections combination. The longitudinal sections are those that parallel to long axis of the fingerprint (z-axis in Fig. 5-1), and the cross-sections are those that perpendicular to it (x-axis in Fig. 5-1). The afferent currents in both conditions were normalized and compared with experimental recorded data from Blake [7]. The reason for choosing Blake's data over these others is due to the similarity in choosing stimulus.

Furthermore, the better combination approach in previous step would be used for predict the afferent current response when the skin model is indented by a 4×4 mm^2

plane. As the experimental data [7] indicates the model should be able to discriminate two edges of indenters larger than 4×4 mm^2. Because the presented model is smaller than indenter, a specific 2-times larger model is developed to complete this task. The larger model is validated by the same methodology as mentioned above (results not shown). The larger model was not used in the first examinations due to two reasons. Firstly, the original model performed well with small indenters, and the dimensions of the original model were sufficient to cover the SED distributions generated by small indenters (see Result section). Secondly, the calculation is very time-consuming and expensive.

5.3 Results

The results from model validation, dynamic response analysis, and synthetic post-processing are shown as below.

5.3.1 Model validation results

Figure 5-3 shows the skin surface deflection when indented by a line indenter, compared with the experimental measurements by Srinivasan [5] and the deflection result from a conventional elastic model by Gerling [4].

The second validation where the obtained SED at SA-1 receptor location are compared with neurophysiological recording, yields R^2 of 0.88. The normalized and fitted SEDs overlay the recorded data [6] in Fig. 5-4.

5.3.2 Mechanical response analysis

The predicted population responses of RA mechanoreceptor (estimated by SED) in vertical displacement process are shown in Fig. 5-5. An interchange zone where the SED varied in peak-valley-peak pattern appeared in all analyses involved with indenter larger than 0.66×0.66 mm^2. The peaks of SED shifted to the apexes of dermal papillae near the edges and corners of the indenter.

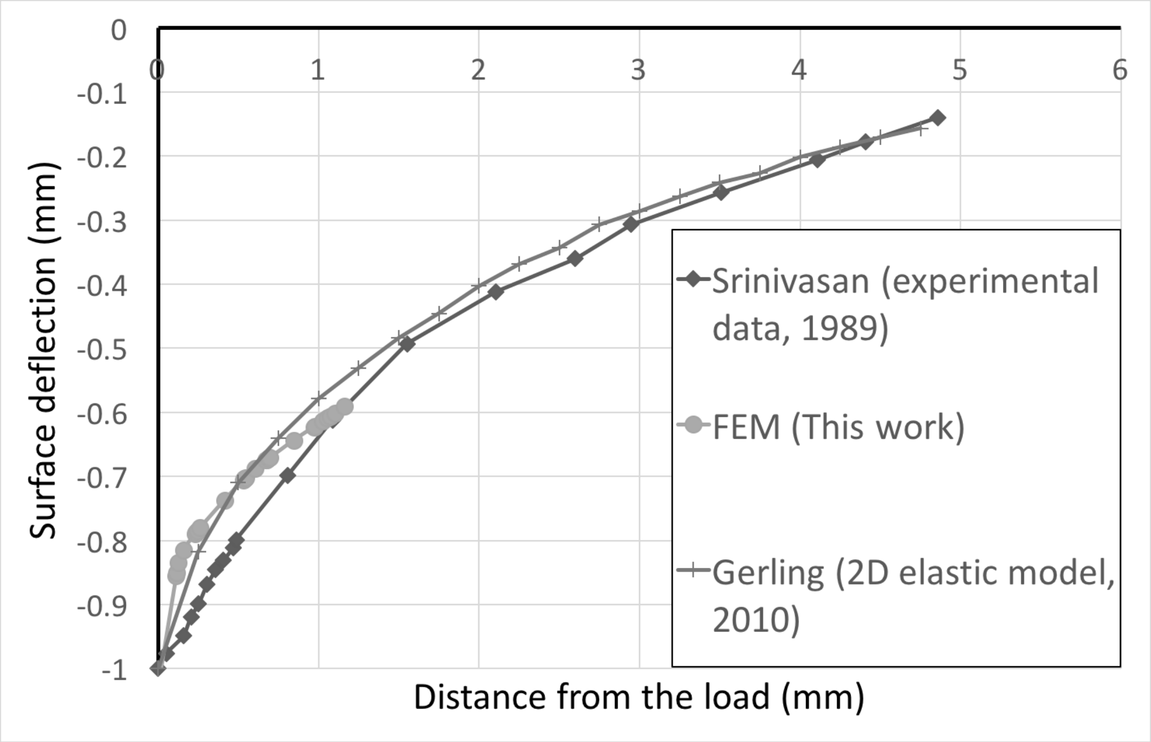

Figure 5-3: Comparison of the predict profile of skin surface with the previously reported model [4] and the experimental data [5]. The indenter was a rigid line.

5.3.3 Synthetic model analysis results

The predicted afferent currents in longitudinal sections combination and cross-sections combination are shown in Fig.5-6 and Fig.5-7; the horizontal axis shows the distance from center of the model in x-axis and z-axis, respectively. In longitudinal sections approach, the difference between peak and valley of interchange zone (as shown in section 3.2) can be seen remarkably reduced after combination. In cross-sections approach, the afferent current profile is similar to the population current profile of receptors in one single section. The goodness of fit (R^2) is 0.95 and 0.90 for the longitudinal sections approach and the cross-sections approach, respectively.

The population response of RA-I receptor to 4×4 mm^2 indenter is shown in Fig.5-8. The SED was transformed into receptor current with parameter from Table 5.2 (longitudinal sections combination) and then summed together. Both predicted responses and observed responses were normalized before compering. An interchange zone can be seen in the middle of both profiles.

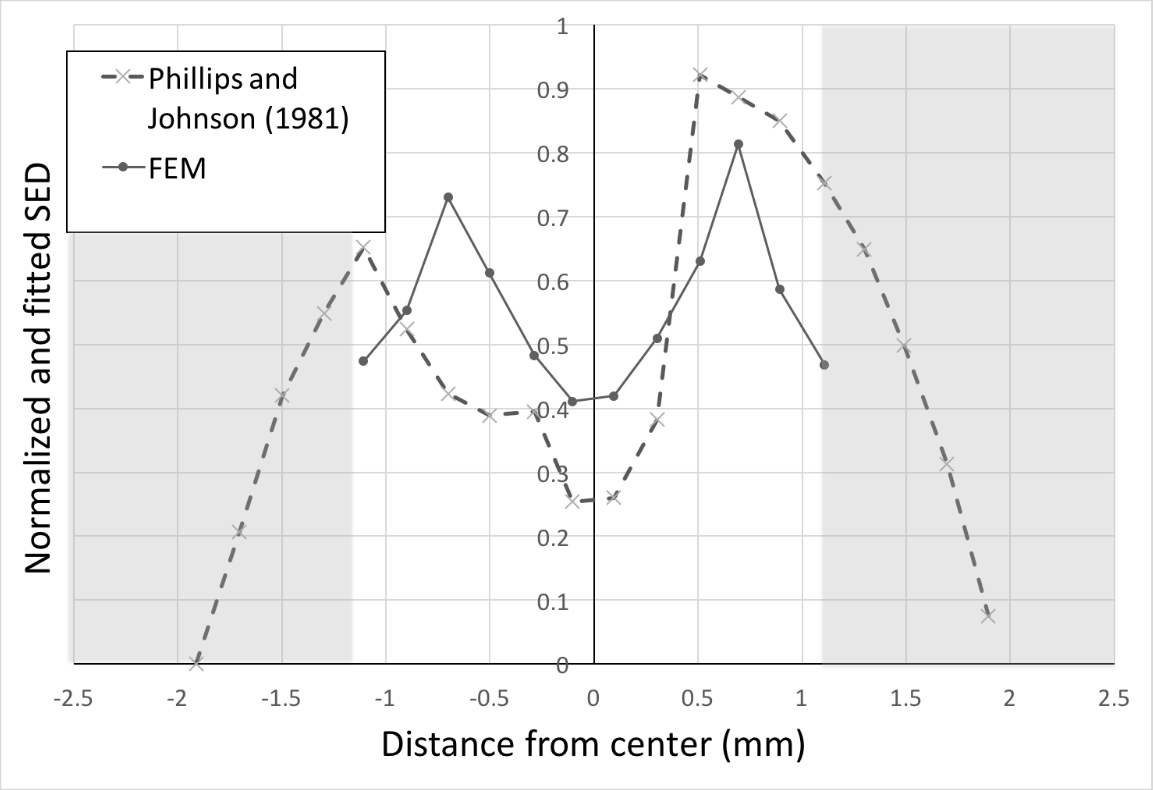

Figure 5-4: Comparison of the normalized and fitted SED profile with the previously reported neurophysiological data [6]. A 2×2 mm^2 plane indenter was placed at the center of the model. The gray indicates the region which is not considered in this work.

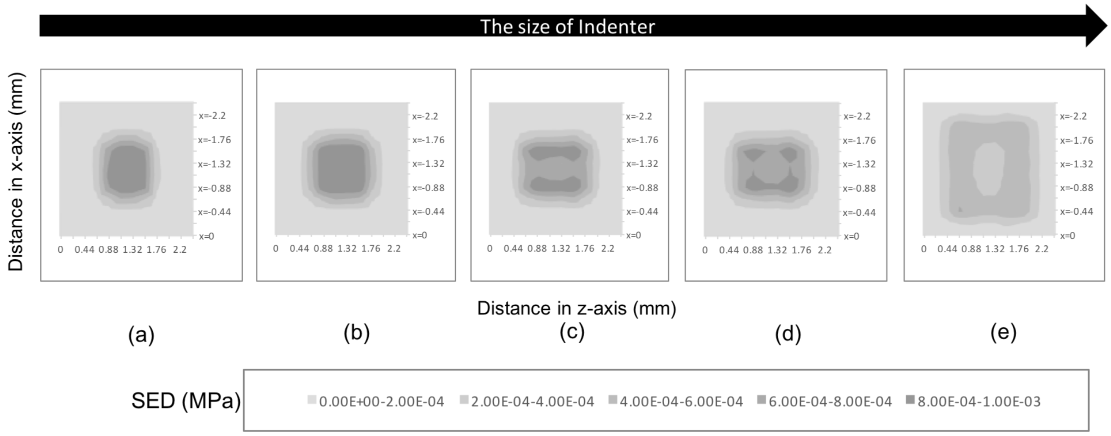

Figure 5-5: Contour of the SED distribution at RA-I receptor location in case of : (a) 0.44×0.44 mm^2, (b) 0.66×0.66 mm^2, (c) 0.88×0.88 mm^2, (d) 1.1×1.1mm^2, (e) 1.32×1.32 mm^2 indenters. The color of bottom squares indicates the magnitude scale of strain energy density (SED) (from left to right, minimum to maximum).

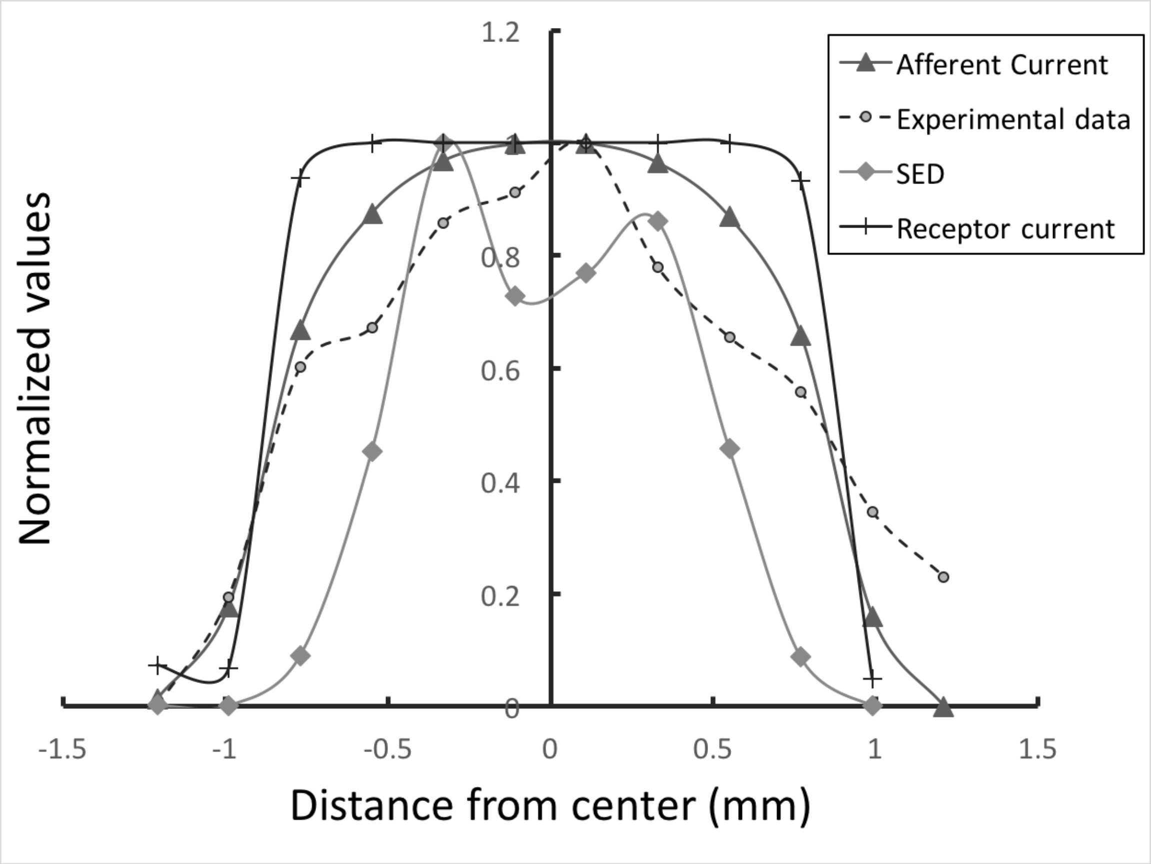

Figure 5-6: Comparison of normalized SED, receptor current, afferent current profiles to experimental data form Blake [7] in the case of longitudinal-section combination. The indenter was $0.88\times088\text{mm}^2$ plane. The horizontal axis shows the distance from center of the model along x-axis.

5.4 Discussion

This work employs a finite-element model of skin mechanics, a sigmoidal transduction function and a synthetic model of receptor current. The elastic behavior of our model was validated through the standard line-load method (Fig.5-3), and showed a good fit to experimental data [5] (especially in the limited range of indenters involved in this study). Another validation method (Fig.5-4) show that our model could be used for neurophysiological data related experiments. Technically, since the conjunction part of epidermis and dermis was complex, we used the free meshing technique in Abaqus software [98] for the whole model (without mirroring). Hence, the mesh was a little asymmetric, resulting the following asymmetric SED profiles as shown in Fig. 5-4,

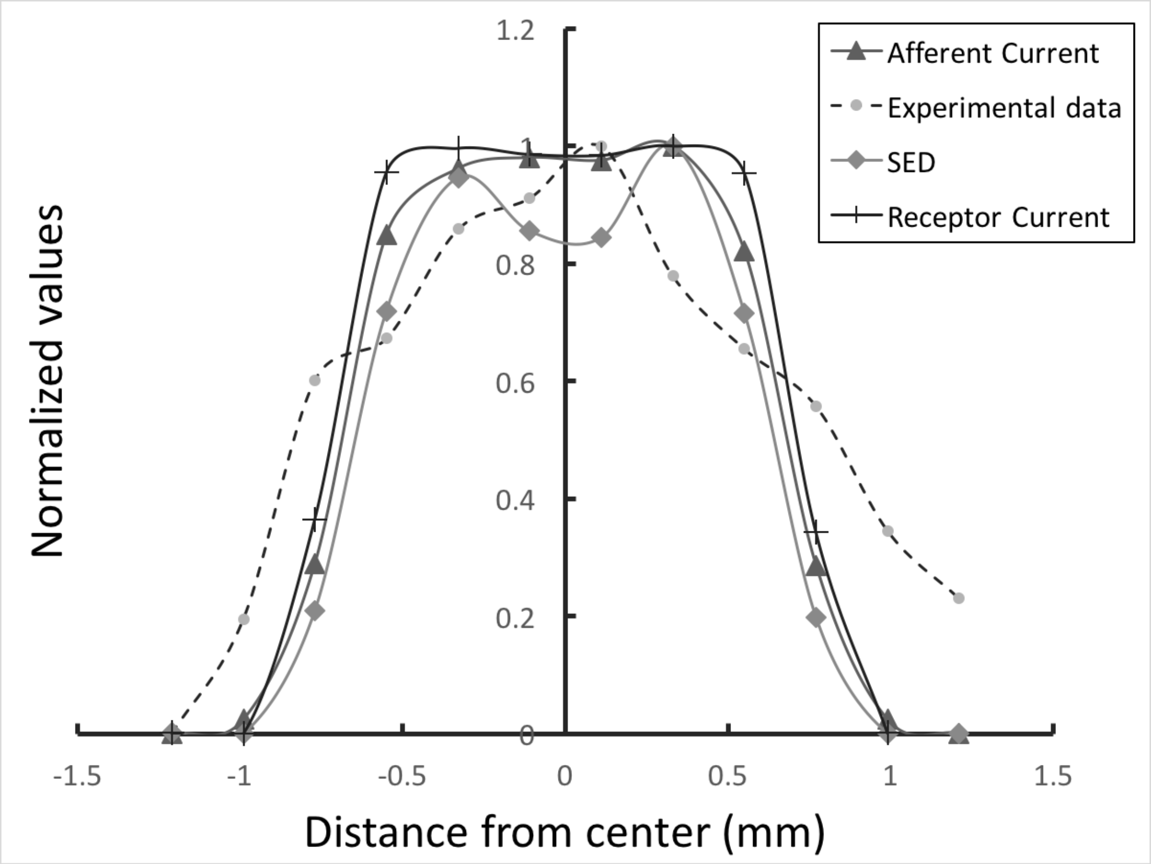

Figure 5-7: Comparison of normalized SED, receptor current, afferent current profiles to experimental data form Blake [7] in the case of cross-section combination. The indenter was $0.88\times088\text{mm}^2$ plane. The horizontal axis shows the distance from center of the model along z-axis.

5-6, and 5-7. In this study, the asymmetric of SED profiles appears to not affect the final result but should be well-aware in future works.

There are two advantages of the presented model in this paper comparing to the others. Firstly, the 3D structure of skin allows us to predict the mechanical response of a population of RA-I receptors at precise positions [94]. Secondly, our model used two additional sub-layers to convert the SED into afferent current. All RA-I receptors were assumed as the electrical components connected in a parallel circuit. Hence, the current of a single-afferent could be extracted as the summation of its related components. Both the anatomical observations and experiment results in this study support this assumption.

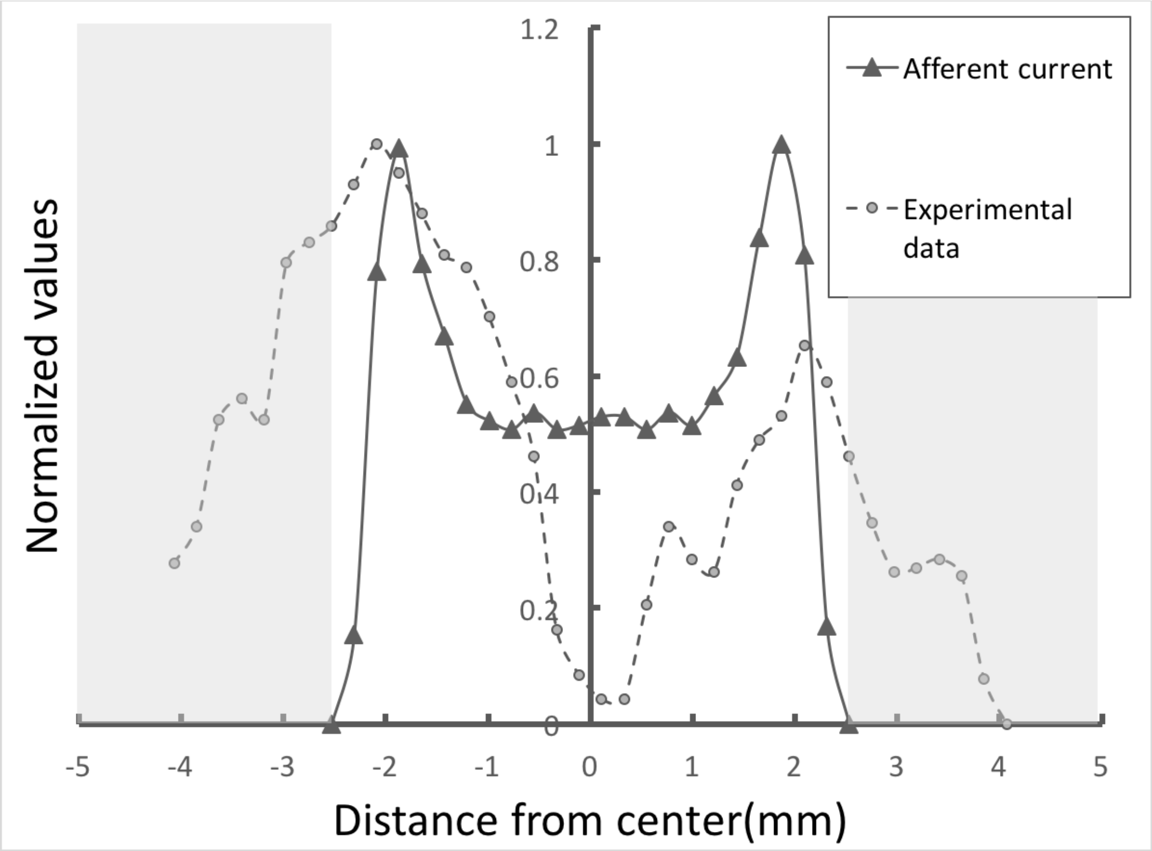

Figure 5-8: Comparison of afferent current profile with the previously reported neurophysiological data [7]. The indenter was 4×4 mm^2 plane. The gray indicates the region which is not considered in this work.

5.4.1 The necessary of transduction layer and synthetic model

An interchange zone can be seen in the SED profile of small indenter (Fig.5-5). Hence, the SED profile appears to highly correlate to the edges of indenter at the widths of 0.88×0.88 mm^2 and larger. The SED profile also appears to be isotropic in most cases. The mechanical response was mismatched the neural recordings of [7] where the RA-I response showed only one peak for the small indenters. This result suggests that the SED is insufficient for explaining the neurophysiological phenomena shown in [7].

On the other hand, the response behavior of afferent current when the width of indenter increased is similar to what was observed in neural recordings of [7]. The synthetic model analysis results a good prediction of the RA-I population response to the plane indentation with various widths (from 0.44 to 4 mm). The model produces a single peak in response profile for small indenter (0.88×0.88 mm^2) as shown in Fig. 5-6 and 5-7, and two separated peaks for large indenter (4×4 mm^2) as shown in Fig. 5-8. The synthetic model of RA-I receptor current into afferent current was examined in two approaches: the longitudinal sections summation and the cross-sections summation. The cross-sections summation shows a modest change in response profile (Fig. 5-7); while the response profile in longitudinal sections summation shows a better fit to the experimental recorded data. This result is expected since the longitudinal sections summation showed a smaller *ssd* that that in the cross-sections summation (Table 5.2). The change of parameters in the longitudinal sections summation was also highly remarkable, suggesting that after RSM process, the transduction sublayer has already preferred the longitudinal sections summation to the cross-sections summation.

Our results support the hypothesis where the specific afferent branching is the major contributor for the uniform response to stimulus smaller than 3×3 mm^2, and the anisotropy in the neural recordings of RA-I afferent [3]. This finding also gets along with the previously anatomical observations in humans [9, 1] and monkey [17] which show the RA receptors connecting to each other in longitudinal sections (along the finger ridges). On other hand, the skin microstructure may contribute to the direction-dependence behavior of afferent current as they have been shown to affect the SED response in [32]. The possible factors include the different lengths of dermal papillae, the different geometry of longitudinal-section and cross-section of fingerprints. Therefore, a further analysis is required to confirm the effect of these factors to the direction-dependence behavior of afferent current.

Interestingly, the difference between response behaviors of SED and afferent current also implies that the neural signal could have been processed at the receptor level through branching method. In term of sensor design, this finding suggests a wiring based approach to pre-process the signal at the sensor level. By which, the amount of data can be reduced before passing to higher levels.

5.4.2 The limitations of proposed model and future works

A technical improvement for investigating population response of RA-I receptor involves with the prediction of firing rate and first spike latency. Recent study [99] shows that the first spike latency, i.e. the time between stimulus onset and the first spike, provides reliable information about direction of fingertip force and object shape faster than rate codes, especially in the case of RA-I afferents. The transformation from SED into firing rate (spikes/time) has been conducted somewhere for SA-I receptors [92] or single RA-I receptor [77]. Those models employ a leaky integrate and fire model to predict the neural spikes and spike times, which result a good fit to experimental data. Note that the leaky integrate and fire model restricts input to vibration magnitude and frequency, thus relevant material parameters (such as the visco-hyperelasticity) should be considered.

Furthermore, the precise combination of receptor current in nature is usually more complex, given that one RA receptor is innervated by multi-neural fibers and one parent fiber already divides multiple times before hand. It indicates that either (1) the cross-effect between neighbor fibers, or (2) the irregular combination at different level of transduction process should be taken into account in future works.

The tiny dimensions and complexity are the major drawbacks of our model. Despite the validation results are equivalent to the others, our model is supposed to be valid in the limited range of indenters (smaller than 2×2 mm^2) owing to the small dimensions. The model also lacks the realistic boundary conditions of skin, since the rigid components of the finger, such as bone and nails, were absent and the coefficient of friction was assumed zero. Our results in this paper are encouraging and should be validated in a larger model where the layers of skin are described in better details, for instance, the full model of a fingertip in [77]. Because each dermal papilla was fixed at the size of 0.11×0.11 mm^2, the calculation could become extremely time-consuming (along with the increased number of dermal papillae) for larger model. One could consider either (1) using an appropriate small number of dermal papillae or (2) employing a neural network for speeding up model predictions.

Chapter 6

Conclusion

This thesis presented our research in two parts: the generation process and the spatial configuration of RA-I receptor.

In the first part, we performed an observation of RA-I receptors (or MC) in vivo by using conventional approach. Since the conventional approach has some limitations such as inconsistency of samples, high-cost, and not interactive, we proposed a less invasive imaging method for afferent axons of MC in the living mouse's fingertip. We confirmed that the mice survived and exhibited no behavioral problems after injection or observation processes. The skin components and the form of the fingertip were kept intact without any signs of burn or damage. Repeated observation was demonstrated over a short period, from PD19 to PD24. These advantages indicate the potential of our approach for examining the development of MC and their mechanical transduction in future work. There are two important findings in this part. Firstly, the observation suggested the important role of the first innervated axon in the development/generation process of MC. Secondly, early result of the two-photon imaging of MC during development period leads us to an idea that dermal events (for instance, the growth of phalanx, the extension of skin) trigger the development of MC globally.

In the second part, we developed a model with the 3D microstructure of skin and compared it with conventional 2D microstructure to examine the effect of natural configuration on the SED distribution of mechanoreceptors. The analysis was conducted with various types of indenters under dynamic conditions. The results indicate that the 3D microstructure modifies the SED at RA-I mechanoreceptors such that it helps in discerning similar indenters (focalizing effect and localizing effect). The 3D microstructure also enhanced the SED response at a RA-I mechanoreceptor when the stimulus frequency increased.

We also developed an extended skin model, combines an FE model of skin mechanics, a sigmoidal function of transduction, and a synthetic sub-model for afferent current for investigating the population response of RA receptors. The current response behavior of our model to various widths of plane indenter is similar to that observed in neural recordings while the mechanical response does not. Two approaches for combining receptor currents into afferent current was examined, i.e. the longitudinal sections approach and the cross-section approach. The longitudinal section approach yields a better result than that in cross-section approach. This result implies the effect of branching method on neural response of RA-I. By which the neural signal can be pre-processed at the receptor level. Our extended model can be used for further investigating the mechanism underlying the population response of RA receptor to many types of stimulus such as depressed patterns, gratings, slipping in future work.

In summary, we have presented a few findings related to generation process (the importance of first deformed axon, simultaneous formation) and spatial configuration (focalizing effect, localizing effect, effect of neural branching method) of RA-I receptor. These findings might be useful for fabrication, structure, and spatial configuration of tactile sensors. We hope these findings could help improve the design of tactile sensors in future works.

Bibliography

[1] Cauna N, Mannan G. Organization and development of the preterminal nerve pattern in the palmar digital tissues of man. J Comp Neur. 1961;117:309–328.

[2] Kumar S, Liu G, Schloerb DW, Srinivasan MA. iscoelastic Characterization of the Primate Finger Pad In Vivo by Microstep Indentation and Three-Dimensional Finite Element Models for Tactile Sensation Studies. ASME J Biomech Eng. 2015;137(6):061002–061002–10.

[3] Bensmaia SJ, Craig JC, Yoshioka T, Johnson KO. SA1 and RA afferent responses to static and vibrating gratings. J Neurophysiol. 2006;95(3):1771–1782.

[4] Gerling GJ. SA-I mechanoreceptor position in fingertip skin may impact sensitivity to edge stimuli. Appl Bionics Biomech. 2010;7(1):19–29.

[5] Srinivasan MA. Surface deflection of primate fingertip under line load. J Biomech. 1989;22(4):343–349.

[6] Johnson KO, Phillips JR. Tactile spatial resolution. I. Two-point discrimination, gap detection, grating resolution, and letter recognition. J Neurophysiol. 1981;46(6):1177–1192.

[7] Blake DT, Johnson KO, Hsiao SS. Monkey cutaneous SA-I and RA responses to raised and depressed scanned patterns: effects of width, height, orientation, and a raised surround. J Neurophysiol. 1997;78(5):2503–2517.

[8] Cauna N. Structure and origin of the capsule of Meissner's corpuscle. Am Rec. 1956;124.

[9] Cauna N. Nerve supply and nerve endings in Meissner's corpuscle. Am J Anat. 1956;99:315–350.

[10] Castano P, Rumio C, Morini M, Miani A Jr, Castano SM. Three-dimensional reconstruction of the Meissner corpuscle of man, after silver impregnation and immunofluorescence with PGP 9.5 antibodies using confocal scanning laser microscopy. J Anat. 1995;186:261–270.

[11] Cauna N. Some observations in the structure and development of Meissner's corpuscle. J Anat. 1953;87:440–441.

[12] Cauna N. Nature and functions of the papillary ridges of the digital skin. Anat Rec. 1954;119:449–468.

[13] Albuerne M, Lavallina JD, Esteban I, Naves F J, Silos-Santiago I, Vega JA. Development of Meissner-Like and Pacinian Sensory Corpuscle in the Mouse Demonstrated With Specific Markers for Corpuscular Constituents. Anat Rec. 2000;258(3):235–242.

[14] Ide C. The fine structure of the digital corpuscle of the mouse toe pad, with special reference to nerve fibers. Am J Anat. 1976;147:329–355.

[15] Vega JA, Llamosas MM, Huerta JJ, Gracia-Fernandez M. Study of human cutaneous sensory corpuscle using double immunolabelling and confocal laser scanning microscopy. Anat Rec. 1996;246:557–560.

[16] Pare M, Elde R, Mazurkiewicz JE, Smith AM, Rice FL. The Meissner corpuscle revised: a multiafferented mechanoreceptor with nociceptor immunochemical properties. J Neurosci. 2001;21(18):7236–7246.

[17] Pare M, Smith A, Rice F. Distribution and terminal arborizations of cutaneous mechanoreceptors in the glabrous finger pads of the monkey. J Comp Neur. 2002;445:347–359.

[18] Guinard D, Usson Y, Guillermet C, and Saxod R. PS-100 and NF 70-200 double immunolabeling for human digital skin Meissner corpuscle 3D imaging. J Histochem Cytochem. 2000;48(2):295–302.

[19] Ide C. Development of Meissner Corpuscle of Mouse Toe Pad. Anat Rec. 1977;188:49–67.

[20] Ide C. Histochemical Study of Lamellar Cell Development of Meissner Corpuscle. Arch Histol Jap. 1981;45:93–97.

[21] Ventura RG, Castano P. Meissner's corpuscle of the green monkey. Electron microscope three-dimensional reconstruction and quantitative analysis of the nervous supply. Acta Anat. 1997;99.

[22] Takahashi-Iwanaga H, Shimoda H. The three-dimensional microanatomy of Meissner corpuscle in monkey palmar skin. J Neurocytol. 2003;32:363–371.

[23] Munger BL, Page RB, Pubols BHJR. Identification of specific mechanosensory receptors in glabrous skin of dorsal root ganglionectomized primates. Anat Rec. 1979;193:630–631.

[24] Johansson RS, Vallbo AB. actile sensibility in the human hand: relative and absolute densities of four types of mechanoreceptive units in glabrous skin. J Physiol. 1979;286:283–300.

[25] Gardner EP, Martin JH, Jessel TM. The bodily senses. In: Principles of Neural Science. 4th ed. Newyork, NY, USA: McGraw-Hill; 2000. p. 430–450.

[26] Zimmerman A, Bai L, Ginty DD. The gentle touch receptors of mammalian skin. Science. 2014;346(6212):950–954.

[27] Kuroki S, Kajimoto H, Nara T, Kawakami N, Taichi S. Consideration of mechanical filtering system of the Meissner corpuscle. In: Proc. SICE Annu Conf; 2008. p. 472–476.

[28] Dandekar K, Raji BI, Srinivasan MA. 3-D Finite Element Models of human and monkey fingertips to investigate the mechanics of tactile sense. ASME J Biomech Eng. 2003;125(5):682–691.

[29] Phillips JR, Johnson KO. Tactile Spatial Resolution. II. Neural. Representation of bars, edges, and gratings in monkey primary afferents. J Neurophysiol. 1981;46(6):1192–1203.

[30] Gerling GJ, Rivest II, Lesniak DR, Scanlon JR, Wan L. Validating a population model of tactile mechanotransduction of slowly adapting type I afferents at levels of skin mechanics, single-unit Response and psychophysics. IEEE Trans Haptics. 2014;7(2):216–228.

[31] Goodwin AW, John KT, Marceglia AH. Tactile discrimination of curvature by humans using only cutaneous information from the fingerpads. Exp Brain Res. 1991;86(3):663–672.

[32] Maeno T, Kobayashi K, Yamazaki N. Relationship between the structure of human finger tissue and the location of tactile receptors. JSME Int J. 1997;41:94–100.

[33] Srinivasan MA, Dandekar K. An investigation of the mechanics of tactile sense using two-dimensional models of the primate fingertip. J Biomech Eng. 1996;118(1):48–55.

[34] Johnson K. The roles and function of cutaneous mechanoreceptors. Current Opinion in Neurobiology. 2001;11(4):455–461.

[35] Phillips JR, Johnson KO. Tactile spatial resolution. II. Neural representation of bars, edges, and gratings in monkey primary afferents. J Neurophysiol. 1981;46(6):1192–1203.

[36] Hao J, Bonnet C, Amsalem M, Ruel J, Delmas P. Transduction and encoding sensory information by skin mechanoreceptors. Pflugers Arch- Eur J Physiol. 2015;467(1):109–119.

[37] Pham PQ, Hoshi T, Tanaka Y, Sano A. Proposal of Tactile Sensor Development Based on Tissue Engineering. In: Proc. of IEEE-RSJ International Conference on Intelligent Robots and System. Tokyo, Japan; 2013.

[38] Hoffman-Kim D, Mitchel JA, Bellamkonda RV. Topography, Cell Response, and Nerve Regeneration. Annu Rev Biomed Eng. 2010;12:203–231.

[39] Ming, G L et al . Adaptation in the chemotactic guidance of nerve growth cones. Nature. 2002;417:441–418.

[40] Patel N, Poo MM. Orientation of Neurite Growth by Extracellular Electric-Fields. J Neurosci. 1982;2:483–496.

[41] Ehrlicher, A et al . Guiding neuronal growth with light. P Natl Acad Sci USA. 2002;99:16024–16028.

[42] Mohanty SK, Sharma M, Panicker MM, Gupta PK. Controlled induction, enhancement, and guidance of neuronal growth cones by use of line optical tweezers. Opt Lett. 2005;30:2596–2598.

[43] Mathew, M et al . Signalling effect of NIR pulsed lasers on axonal growth. J Neurosci Meth. 2010;186:196–201.

[44] Wu, T et al . Neuronal growth cones respond to laser-induced axonal damage. Journal of The Royal Society Interface. 2012;9:535–547.

[45] Blau, A et al . Promotion of neural cell adhesion by electrochemically generated and functionalized polymer films. J Neurosci Meth. 2001;112:65–73.

[46] Wu, T et al . A photo-driven micromotor can direct nerve fibre growth. Nature Photonics. 2012;6:62–67.

[47] Luo Y, Shoichet MS. A photolabile hydrogel for guided three-dimensional cell growth and migration. Nat Mater. 2004;3:249–253.

[48] Herrmann DN, Boger JN, Jansen C, Alessi-Fox C. In vivo confocal microscopy of Meissner corpuscle as a measure of sensory neuropathy. Neurology. 2007;69:2121–2127.

[49] Almodovar JL, Ferguson M, McDermott MP, Lewis RA, Shy ME, Herrmann DN. In vivo confocal microscopy of Meissner corpuscle as a novel sensory measure in CMTLA. J Peripher Nerv Syst. 2011;16:169–174.

[50] Denk W, Strickler JH, Webb WW. Two-photon laser scanning fluorescence microscopy. Science. 1990;248:74–76.

[51] Masters BR, So PTC, Gratton E. Multiphoton exciation fluorescence microscopy and spectroscopy of in vivo human skin. Biophys J. 1997;72:2405–2412.

[52] Helmchen F, Denk W. Deep tissue two-photon microscopy. Nat Methods. 2005;2:932–940.

[53] Grutzendler J, Narayanan K, Gan WB. Long-term dendritic spine stability in adult cortex. Nature. 2002;420:812–816.

[54] Grutzendler J, Yang G, Pan F, Parkhurst CN, Gan W. Transcranial two-photon imaging of the living mouse brain. Cold Spring Harb Protoc. 2011; p. 1080–1088.

[55] Yoder EJ, Kleinfeld D. Cortical Imaging Through the Intact Mouse Skull Using Two-Photon Exciation Laser Scanning Microscopy. Microsc Res Tech. 2002;56:304–305.

[56] Holtmaat A, Bonhoeffer T, Chow DK, Chuckowree J, Paola VD, Hofer SB, et al. Long term, high-resolution imaging in the mouse neocortex through a chronic cranial window. Nat Protoc. 2009;4:1128–1144.

[57] Amit S, Yaron A. Novel systems for in vivo monitoring and microenvironmental investigations of diabetic neuropathy in a murine model. J Neural Transm. 2012;119:1317–1325.

[58] Renehan WE, Munger BL. The development of Meissner corpuscle in primate digital skin. Dev Brain Res. 1990;51:35–44.

[59] Johnson D. Section 6: Pectoral girdle and upper limb. In: Standring S, Borley NR, editors, editor. Gray's Anatomy: The anatomical basis of clinical practice. 14th ed. London: Elsevier; 2008. p. 775–905.

[60] Perrom FE, Stoeckli ET. Use of lipophilic dyes in studies of axonal pathfinding in vivo. Microsc Res Tech. 2000;48:25–31.

[61] Fishell G, Blazes R, Godement P, Rivas R, Wang LC, Mason CA. Tracking fluorescently labeled neurons in developing brain. Faseb J. 1995;9:324–334.

[62] Godement P, Vanselow J, Thanos S, Bonhoeffer F. A study in developing visual systems with a new method of staining neurons and their processes in fixed tissue. Development. 1987;101:697–713.

[63] Kim BG, Dai HN, McAtee M, Vicini S, Bregman BS. Labeling of Dendritic Spines with The Carbocyanine dye DiI for Confocal Microscopic Imaging in Lightly Fixed Cortical Slices. J Neurosci Methods. 2007;162(1-2):237–243.

[64] Fischer G, Kostic S, Nakai H, Park F, Sapunar D, Yu H, et al. Direct injection into the dorsal root ganglion: Technical, behavioral, and histological observations. J Neurosci Methods. 2011;199:43–55.

[65] Carmeliet P, Tessier-Lavigne M. Common mechanisms of nerve and blood vessel wiring. Nature. 2005;436:193–200.

[66] Schindelin J, Arganda-Carreras I, Frise E, Kaynig V, Longair M, Pietzsch T, et al. Fiji: an open-source platform for biological image analysis. Nat Methods. 2012;9:676–682.

[67] Longair MH, Baker DA, Amstrong JD. Simple Neurite Tracer: Open Source software for reconstruction, visualization and analysis of neuronal processes. Bioinf. 2011;27:2453–2454.

[68] Mitsuhiro H, Hideki O, Hiroyuki S. Telemetric Robot Skin. In: Proc. 1999 IEEE International Conference on Robotics and Automation. Detroit, Michigan; 1999. p. 957–961.

[69] Murabayashi M, Minato M, Okuhata T, Makimoto M, Hosono S, Masaoka N, et al. Kinetics of Serum S100B in Newborns with Intracranial Lesions. Pediatr Int. 2008;50:17–22.

[70] Li Y, Song Y, Zhao L, Gaidosh G, Katies AM, Wen R. Direct labeling and visualization of blood vessels with lipophilic carbocyanine dye DiI. Nat Protoc. 2008;3(11):1703–1708.

[71] Sano H, Sudo T, Yokode M, Murayama T, Kataoka H, Takakura N, et al. Functional Blockade of Platelet-Derived Growth Factor Receptor- beta but Not of Receptor- alpha Prevents Vascular Smooth Muscle Cell Accumulation in Fibrous Cap Lesions in Apolipoprotein E-Deficient Mice. Circulation. 2001;103:2955–2960.

[72] Marcia GH, Richard IH. Fluorescent Carbocyanine Dyes Allow Living Neurons of Identified Origin to Be Studied in Long-Term Cultures. J Cell Biol. 1986;103:171–187.

[73] Vega JA, Lopez-Muniz A, Calavia MG, Garcia-Suarez O, Cobo J, Otero J, et al. Clinical Implication of Meissner's Corpuscle. CNS Neurological Disorders-Drug Targets. 2012;11(7):856–868.

[74] Vallbo AB, Hagbarth KE, Wallin BG. Microneurography: how the technique developed and its role in the investigation of the sympathetic nervous system. J Appl Physical. 2004;96:1262–1269.

[75] Kunimoto M. Additional Further Application of Microneurography in the Future. Brain Nerve. 2009;61(3):277–284.

[76] Wigley C. Skin and its appendages. In: Standring S, Borley NR, editors, editor. Gray's Anatomy: The anatomical basis of clinical practice. 14th ed. London: Elsevier; 2008. p. 145–157.

[77] Vodlak T, Vidrih Z, Pirih P, Skorjanc A, Presern J, Rodic T. Functional Microanatomical Model of Meissner Corpuscle - From Finite Element Model to Mechano-Transduction. In: Auvray M, Duriez C, editors. EuroHaptics (2). vol. 8619 of Lecture Notes in Computer Science. Springer; 2014. p. 377–384.

[78] Adams MJ, Johnson SA, Lefèvre P, Lévesque V, Hayward V, André T, et al. Finger pad friction and its role in grip and touch. J R Soc Interface. 2013;10(80). doi:10.1098/rsif.2012.0467.

[79] Fung YC. Biomechanics-mechanical properties of living tissue. 2nd ed. Springer-Verlag; 1993.

[80] Wu JZ, Dong RG, Rakheja S, Schopper AW, Smutz WP. A structural fingertip model for simulating of the biomechanics of tactile sensation. Med Eng Phys. 2004;26(2):165 – 175. doi:https://doi.org/10.1016/j.medengphy.2003.09.004.

[81] Ge W, Khalsa PS. Encoding of compressive stress during indentation by slowly adapting type-i mechanoreceptors in rat hairy skin. J Neurophysiol. 2002;87(4):1686–1693.

[82] Molski K, Glinka G. A method of elastic-plastic stress and strain calculation at a notch root. Mater Sci Eng. 1981;50(1):93 – 100. doi:https://doi.org/10.1016/0025-5416(81)90089-6.

[83] Talbot WH, Smith ID, Kornhuber HH, Mountcastle VB. The sense of flutter-vibration: comparison of the human capacity with response patterns of mechanoreceptive afferents from the monkey hand. J Neurophysiol. 1968;31(2):301–334.

[84] Harih G, Tada M, Dolšak B. Justification for a 2D versus 3D fingertip finite element model during static contact simulations. Comput Methods Biomech Biomed Engin. 2016;19(13):1409–1417. doi:10.1080/10255842.2016.1146712.

[85] Gerling GJ, Thomas GW. The effect of fingertip microstructures on tactile edge perception. In: Proc. First Joint Eurohaptics Conf. Symp. Haptic Interfaces Virtual Environ. Teleoperator Syst; 2005. p. 63–72.

[86] Dahiya RS, Metta G, Valle M, Sandini G. Tactile sensing- from humans to humanoids. IEEE Trans Robotics. 2010;26(1):1–20.

[87] Shimojo M. Spatial filtering characteristic of elastic cover for tactile sensor. In: IEEE Proc. of Robotics and Automation; 1994. p. 287–292.

[88] Zhang Y, Miki N. Sensitivity enhancement of a micro-scale biomimetic tactile sensor with epidermal ridges. J Micromech Microeng. 2010;20(12):129801.

[89] Salehi S, Cabibihan JJ, Ge SS. Artificial skin ridges enhance local tactile shape discrimination. Sensors. 2010;11:8626–8642.

[90] Vasarhelyi G, Adam M, Vazsonyi E, Barsony I, Ducso C. Effects of the elastic cover on tactile sensor arrays. Sens Actuat A Phys. 2006;132:245–251.

[91] Chorley C, Melhuish C, Pipe T, Rossiter J . Development of a tactile sensor based on biologically inspired edge encoding. In: Proc. of IEEE International Conference on Advanced Robotics; 2009. p. 1–6.

[92] Lesniak DR, Gerling GJ. Predicting SA-I mechanoreceptor spike times with a skin-neuron model. Math Biosci. 2009;220(1):15–23.

[93] Somer DD, Peric D, de Souza Neto EA, Dettmer WG. A multi-scale computational assessment of channel gating assumptions within the Meissner corpuscle. J Biomech. 2015;48(1):73–80.

[94] Pham TQ, Hoshi T, Tanaka Y, Sano A. A Finite Element Model of 3D Microstructure of Dermal Papillae: Concentration of Strain Energy Density at Mechanoreceptor Locations. In: Proc. SICE Annu Conf; 2016. p. 1320–1322.

[95] Holt JR, Corey DP. Two mechanisms for transducer adaption in vertebrate hair cells. PNAS. 2000;97(2):11730–11735.

[96] Siemens J, Zhou S, Piskorowski R, Nikai T, Lumpkin EA, Basbaum AI, et al. pider toxins active the capsaicin receptor to produce inflammatory pain. Nature. 2006;444(7116):208–212.

[97] Myers RH, Montgomery DC. Response Surface Methodology. 2nd ed. Wiley-Interscience; 2002.

[98] ABAQUS. ABAQUS Documentation; 2016.

[99] Johansson RS, Birznieks I. First spikes in ensembles of human tactile afferents code complex spatial fingertip events. Nat Neurosci. 2004;7(2):170–177.

Related publications

Journals

1. T.Q. Pham, T. Hoshi, Y. Tanaka, A.Sano, T. Miyata, and T. Kawaue, Two-photon Imaging of DiO-labelled Meissner Corpuscle in Living Mouse ś Fingertip, IEEE Transactions on Haptics, 2016, Vol. 9, No. 4, pp. 483-491.

2. T.Q. Pham, T. Hoshi, Y. Tanaka, A. Sano, An FE simulation study on population response of RA-I mechanoreceptor to different widths of square indenter, SICE Journal of Control, Measurement, and System Integration, Vol.10, No. 5, pp. 426-432, 2017.

3. T.Q. Pham, T. Hoshi, Y. Tanaka, A. Sano, Effect of 3D Microstructure of dermal papillae on SED concentration at a mechanoreceptor location, PLOS ONE, Vol. 12, No. 12, e0189293, 2017.

Proceedings of International Conferences

1. P. Q. Trung, T. Hoshi, Y. Tanaka, A. Sano, Proposal of Tactile Sensor Development Based on Tissue Engineering, Proc. Of IEEE-RSJ International Conference on Intelligent Robots and System 2013 (IROS 2013), Tokyo, Japan, April 2013.

2. P. Q. Trung, T. Hoshi, Y. Tanaka, A. Sano, Investigation of Spatial Structure Surrounding Meissner Corpuscle by Using Compact Finite-Element Methods, Proc. Of the 7th Vietnamese and Japanese Student Scientific Exchange Meeting (VJSE2014), Kobe, Japan, October 2014.

3. P. Q. Trung, T. Hoshi, Y. Tanaka, A. Sano, Study on Three-dimensional Configuration of Dermal Papillae: Effect on Meissner Corpuscle, Proc. Of the 6th IEEE World Haptics Conference 2015 (Work-In-Progress section), Chicago, USA, June 2015.

4. P. Q. Trung, T. Hoshi, Y. Tanaka, A. Sano, Investigation on Tactile Sensor Development based on Tissue Engineering, Proc. Of the 8th Vietnamese and Japanese Student Scientific Exchange Meeting (VJSE2015), Kyoto, Japan, October 2015.

5. P. Q. Trung, T. Hoshi, Y. Tanaka, A. Sano, A Finite Element Model of 3D Microstructure of Dermal Papillae: Concentration of Strain Energy Density at Mechanoreceptor Locations, Proc. Of SICE Annual Conference 2016 (SICE2016), Tsukuba, Japan, September 2016.

Proceedings of National Conferences

1. P. Q. Trung, T. Hoshi, Y. Tanaka, A. Sano, Consideration of Generation Process of Meissner Corpuscle, Proc. Of the 13th SICE System Integration Division Annual Conference (SI 2012), Fukuoka, Japan, December 2012. (In Japanese)
2. T. Hoshi, P. Q. Trung, Y. Tanaka, A. Sano, Consideration of Spatial Configuration of Meissner Corpuscles, Proc. Of the 13th SICE System Integration Division Annual Conference (SI 2012), Fukuoka, Japan, December 2012. (In Japanese)
3. P. Q. Trung, T. Hoshi, Y. Tanaka, A. Sano, Consideration of Generation Process of Meissner Corpuscle (2nd Report), Proc. Of the 14th SICE System Integration Division Annual Conference (SI 2013), Kobe, Japan, December 2013. (In Japanese)
4. T. Hoshi, P. Q. Trung, Y. Tanaka, A. Sano, Consideration of Spatial Configuration of Meissner Corpuscles (2nd Report), Proc. Of the 14th SICE System Integration Division Annual Conference (SI 2013), Nagoya, Japan, December 2013. (In Japanese)
5. P. Q. Trung, T. Hoshi, Y. Tanaka, A. Sano, Consideration of Generation Process of Meissner Corpuscle (3rd Report), Proc. Of the 15th SICE System Integration Division Annual Conference (SI 2014), Tokyo, Japan, December 2014. (In Japanese)
6. T. Hoshi, P. Q. Trung, Y. Tanaka, A. Sano, Consideration of Spatial Configuration of Meissner Corpuscles (3rd Report), Proc. Of the 15th SICE System Integration Division Annual Conference (SI 2014), Tokyo, Japan, December 2014. (In Japanese)
7. P. Q. Trung, T. Hoshi, Y. Tanaka, A. Sano, Consideration of Generation Process of Meissner Corpuscle (4th Report), Proc. Of the 16th SICE System Integration Division Annual Conference (SI 2015), Nagoya, Japan, December 2015. (In Japanese)
8. T. Hoshi, P. Q. Trung, Y. Tanaka, A. Sano, Consideration of Spatial Configuration of Meissner Corpuscles (4th Report), Proc. Of the 16th SICE System Integration Division Annual Conference (SI 2015), Nagoya, Japan, December 2015. (In Japanese)
9. P. Q. Trung, T. Hoshi, Y. Tanaka, A. Sano, Consideration of Generation Process of Meissner Corpuscle (5th Report), Proc. Of the 17th SICE System Integration Division Annual Conference (SI 2016), Hokkaido, Japan, December 2016. (In Japanese)